

We are IntechOpen, the world's leading publisher of Open Access books Built by scientists, for scientists

6,900

Open access books available

186,000

International authors and editors

200M

Downloads

Our authors are among the

154

Countries delivered to

TOP 1%

most cited scientists

12.2%

Contributors from top 500 universities



WEB OF SCIENCE™

Selection of our books indexed in the Book Citation Index
in Web of Science™ Core Collection (BKCI)

Interested in publishing with us?
Contact book.department@intechopen.com

Numbers displayed above are based on latest data collected.
For more information visit www.intechopen.com



FE Analysis of Evolution of Defects during Rolling

Dr. YU Hai-liang^{1,2}

¹Key Laboratory for Advanced Materials Processing Technology of Ministry of Education,
Department of Mechanical Engineering, Tsinghua University,
Beijing 100084
China

² State Key Laboratory of Rolling and Automation, Northeastern University,
Shenyang 110004
China

Finite element method (FEM) has been widely employed for simulation of rolling problems, such as thermal field [1,2], stress-strain field [3], microstructure distribution [4], rolling force [5], rolling pressure distribution [6], plate view shape [7,8], roll deflection [9,10], tracing the evolution of macrosegregation [11]. As the development of FEM, there are three important ways for the application of FEM in analysis of rolling problems recently. Firstly, rapid FEM, and its on-line application [12-14]; secondly, coupled multi-scale FEM, macro - FEM & micro - FEM & crystal - FEM, coupled the macro-deformation and microstructure evolution and texture distribution [15-16]; third, tracing the defects in whole rolling processes [11, 18-21].

Defects might appear in materials, such as cracks, inclusions. The evolution behavior of defects in steels during rolling severely affects the rolled products quality. In this chapter, the author summed up the previous researches on the evolution of cracks and inclusions during rolling, mainly contains the researches on the evolution of surface cracks by 2D thermo-mechanical FEM, the evolution of surface cracks during vertical-horizontal (V-H) rolling by 3D FEM, the evolution of internal cracks during V-H rolling, the evolution of inclusions during flat rolling.

1. Evolution of surface cracks by 2D thermo-mechanical FEM

Since the brittle fracture model proposed by Griffith last century, a large number of researchers and engineers have carried out a lot of work that focuses on the behavior of cracks. The research reports on the appearance and the propagation of cracks in rolled steels during rolling were investigated [22~25].

Considerable investigations have been carried out on applying FEM for simulation of the propagation and closure of cracks in materials during rolling. A self-healing shape memory alloy (SMA) composite was simulated via a finite element approach that allows crack to propagate in a brittle matrix material by Burton, et al [26]. The SMA wires were carefully

modeled using a one-dimensional SMA constitutive model and implemented into user-defined truss elements. Loading of the composite allowed a crack to propagate from an initiation site and the wires bridge the crack as detwinned martensite forms with the applied loading. Awais [27] and Son et al [28] employed the two-dimension FEM and Processing Map to analyze the closure and growth of surface crack in bars in the rolling process. Ervasti, et al [29, 30] simulated the closure and growth of longitudinal and transversal cracks in flat rolling process, and analyzed the closure and growth of cracks under a variety of the crack sizes, roll radii, friction coefficients, etc. Yukawa, et al [31, 32] analyzed the deformation of the micro-cracks, the foreign bodies pressing and so on in rolling process by a two-dimensional (2D) rigid-plastic FE code developed by them. In this part, the researches on the evolution of surface cracks by 2D thermo-mechanical FEM are carried out.

1.1 Finite element method

1.1.1 Basic theory

Eq. (1) [33] shows the calculation equation of thermal distribution in an isotropic element with an internal heat source.

$$\frac{\partial^2 T}{\partial x^2} + \frac{\partial^2 T}{\partial y^2} + \frac{\partial^2 T}{\partial z^2} + \frac{\dot{q}}{k} = \frac{\rho c}{k} \frac{\partial T}{\partial t} \quad (1)$$

where ρ is density; c is specific heat; k is coefficient of heat conductivity; \dot{q} is internal heat source strength, which is the plastic work done of slab deformation during rolling.

$$\dot{q} = m \int_0^{\dot{\epsilon}} \bar{\sigma} d\dot{\epsilon} \quad (2)$$

where m is coefficient of heat transform by plastic work done, $m = 0.7 \sim 0.95$ [34].

During hot rolling, the thermal transfers between the slab surface and the external environment contain two ways: heat emission and convection current. When the slab is not in the deformation zone, the heat radiation is much larger than the heat convection which could be neglected. According to the Stefan-Boltzman equation,

$$Q = H_r A (T - T_\infty) \quad (3)$$

where $H_r = S_B B_S (T^2 + T_\infty^2)(T + T_\infty)$, S_B is the coefficient of Stefan-Boltzman; B_S is the blackness on slab surface, T is the slab surface temperature; T_∞ is the temperature of environment.

The heat transfers between the slab surface and the work roll is calculated by the Eq. (4).

$$Q = h_i A (T - T_R) \quad (4)$$

where h_i is the coefficient of convective heat transfer between the slab and the roll; T_R is the temperature of roll.

The coupled thermal-mechanical method is solved by dynamic explicit approach [35].

The heat transfer equations are integrated using the explicit forward-difference time integration rule:

$$\theta_{i+1}^N = \theta_i^N + \Delta t_{i+1} \dot{\theta}_i^N \quad (5)$$

where θ^N is the temperature at node N and the subscript i refers to the increment number in an explicit dynamic step. The values of $\dot{\theta}_i^N$ are computed at the beginning of the increment by

$$\dot{\theta}_i^N = (C^{NJ})^{-1} (P_i^J - F_i^J) \quad (6)$$

where C^{NJ} is the lumped capacitance matrix, P^J is the applied nodal source vector, and F^J is the internal flux vector.

The equations of motion for the body are integrated using the explicit central-difference integration rule

$$\dot{u}_{i+\frac{1}{2}}^N = \dot{u}_{i-\frac{1}{2}}^N + \frac{\Delta t_{i+1} + \Delta t_i}{2} \ddot{u}_i^N \quad (7)$$

$$u_{i+1}^N = u_i^N + \Delta t_{i+1} \dot{u}_{i+\frac{1}{2}}^N \quad (8)$$

where u^N is a degree of freedom (a displacement or rotation component) at node N. The accelerations at the beginning of the increment are computed by

$$\ddot{u}_i^N = (M^{NJ})^{-1} (P_i^J - I_i^J) \quad (9)$$

where M^{NJ} is the mass matrix, P^J is the applied load vector, and I^J is the internal force vector.

1.1.2 Parameters and FE model

Fig.1 shows the schematic drawing of slab rolling with a surface crack. In the models, the work roll diameter (D_W) is 1 150 mm, the slab thickness before rolling (H_0) is 250 mm, and the slab thickness after rolling (H_1) is 230 mm. The cracks are assumed to be V-shaped. There are two important parameters for definition of the crack: crack height (H_C), and crack open-angle (θ), whose effects on the behavior of cracks during rolling are analyzed. The values of H_C are assumed to be 2 mm, 4 mm, 6 mm, 8 mm, and 10 mm respectively. The values of θ are assumed to be 5°, 10°, 20°, 30°, 40° separately.

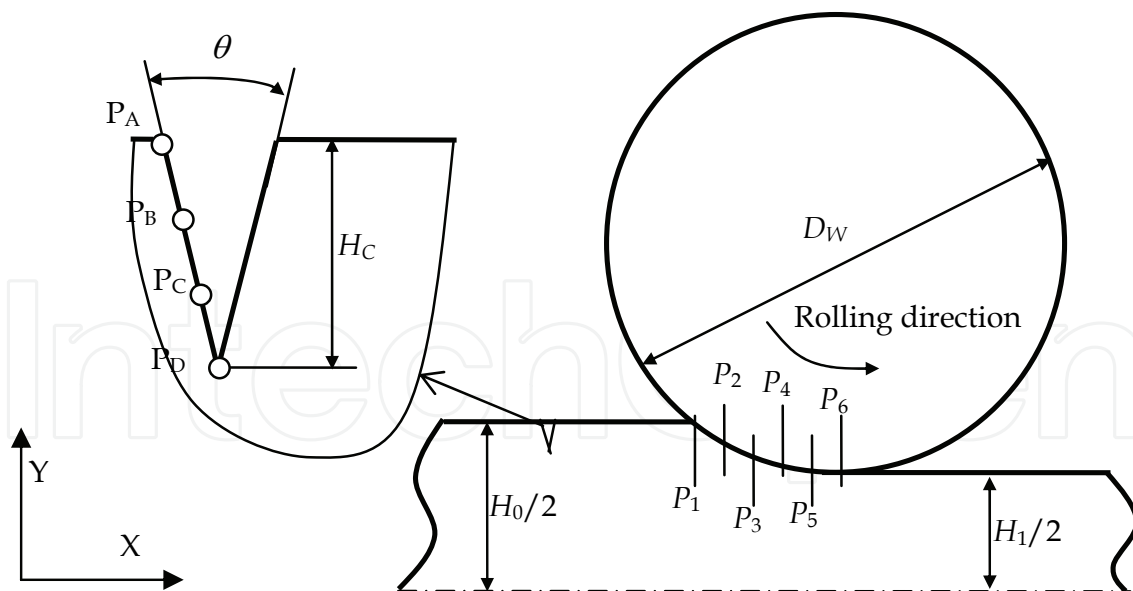


Fig. 1. Schematic drawing of slab rolling with a surface crack

The Coulomb friction model is used for solving the pressure between the crack surfaces and that between the slab and the roll. The influence of friction factor between the slab and the roll on the behavior of cracks during rolling are analyzed. The friction coefficients are assumed to be 0.2, 0.25, 0.35, 0.45, and 0.55.

The heat transfer between the slab and the roll, and between the crack surfaces are appeared, where the heat conductivity is assumed to be constant 46 W/m·K. During rolling, the deformation resistance of slab is related with the strain, strain rate, and temperature. The roll is assumed to be rigid, and the slab is isotropic bilinear model. The main material parameters are shown in **Table 1**.

Parameters	Roll	Slab
Density, kg/m ³	7830	7830
Young's modulus, GPa	210	117
Poisson's ratio	0.3	0.36
Deformation resistance, MPa	-	$\sigma = A \varepsilon^B \dot{\varepsilon}^{CT+D} e^{FT}$
Heat capacity, J/(kg·K)	460	460

Table 1. Material parameters (σ is stress; ε is true strain; $\dot{\varepsilon}$ strain rate; A, B, C, D, and F are constants)

Owing to the symmetry of the rolls and the slab, a half of rolling geometrical model is employed. During rolling, the width spread of slab in a local zone is small, where the behavior of cracks could be approximate as the 2D deformation, so a 2D geometrical model is used. With the parameters above, the models of slab rolling with a surface crack are established, which are meshed by the quadrilateral elements. The FE meshing of slab with a surface crack during rolling is shown in **Fig.2**. The nodes on the bottom of slab are constrained for displacement along slab thickness direction, $U_Y = 0$. During rolling, the slab enters the roll with an initial velocity, and exits under the action of friction force between the roll and the slab.

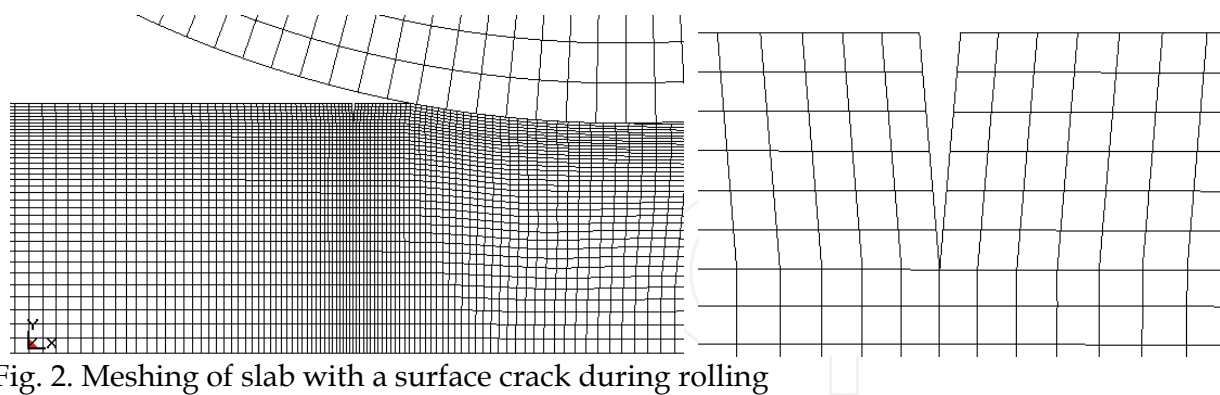


Fig. 2. Meshing of slab with a surface crack during rolling

1.2. Results and discussion [36]

1.2.1 Stress around crack tip during rolling

Fig. 3 shows the stress (σ_x) distribution around the crack at different positions in the deformation zone during rolling when the initial crack height is 10 mm, the initial crack open-angle is 10° and the friction coefficient is 0.35. In the bite zone, the compressive stress appears around the crack, and the crack gradually close, as shown in **Fig.3** (a) ~ (c). In **Fig.3** (d), the stress around crack is small, and the crack keeps its shape. When the crack is in the

forward zone, the tensile stress appears around cracks, and when the crack is at P_6 , the maximum tensile stress around crack tip attaches to 900 MPa, as shown in Fig.3 (e) and (f). It is obvious that the larger the compressive stress is, the more easily the cracks close, and the larger the tensile stress is, the more easily the cracks propagate. The maximum compressive stress and the maximum tensile stress at crack tip during rolling are further analyzed as follows.

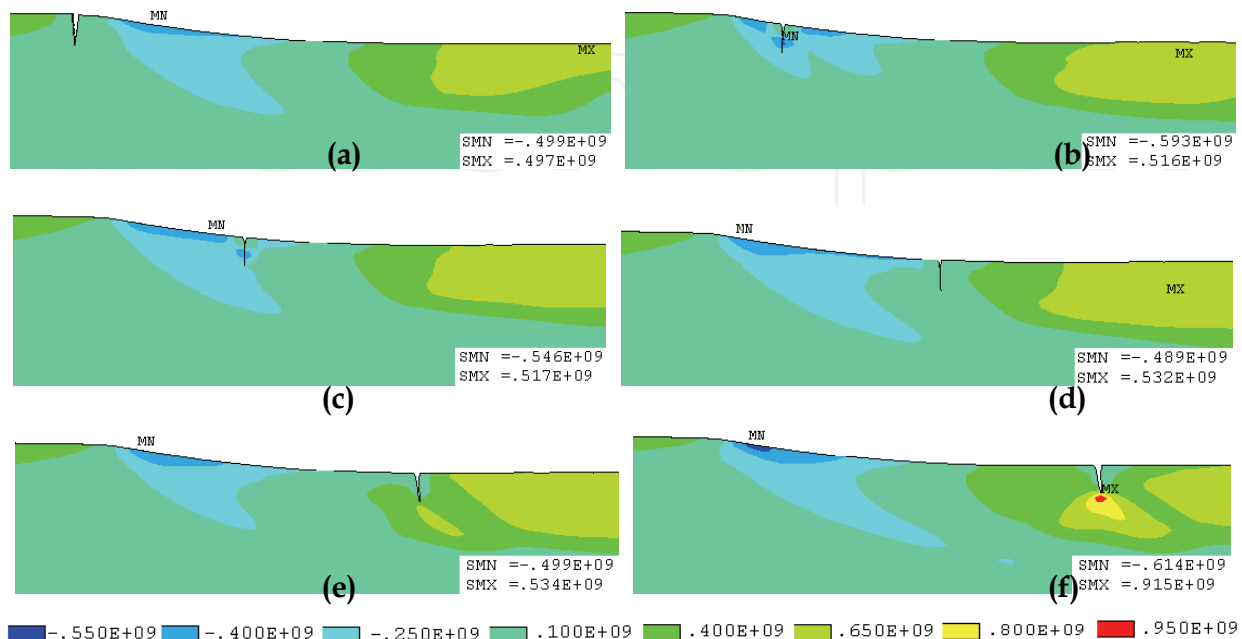


Fig. 3. Stress distribution around the crack at P_1 (a), P_2 (b), P_3 (c), P_4 (d), P_5 (e) and P_6 (f) in the deformation zone

Fig. 4 shows the maximum compressive and tensile stress at crack tip during rolling under various initial crack heights when the friction coefficient is 0.35 and the initial crack open-angle is 10° . As the initial crack height decreases, the maximum compressive stress increases. By contraries, the maximum tensile stress increases as the initial crack height increases.

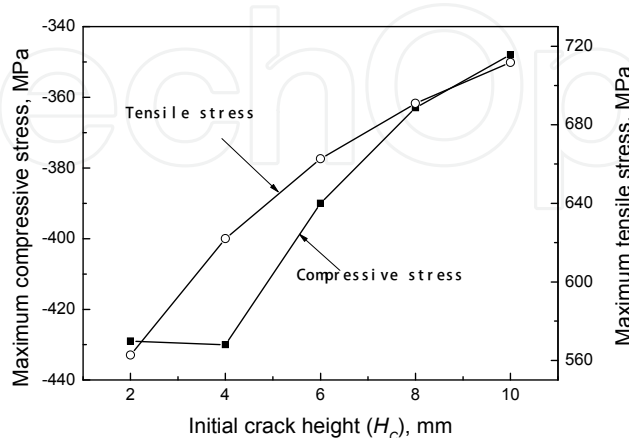


Fig. 4. Maximum compressive and tensile stress at crack tip during rolling for various H_c

Fig. 5 shows the maximum compressive and tensile stress at crack tip for a variety of initial crack open-angles when the friction coefficient is 0.35 and the initial crack height is 10 mm. With increasing the initial crack open-angle, the compressive stress increases. Under the rolling conditions, the maximum tensile stress decreases as the initial crack open-angle increases when the crack open-angle is 5~20°, which increases when the crack open-angle is between 20~40°.

Fig. 6 shows the maximum compressive and tensile stress at crack tip under different friction coefficients when the initial crack height is 10 mm and the initial crack open-angle is 10°. The maximum compressive stress increases with decreasing the friction coefficients. The maximum tensile stress increases with increasing the friction coefficients when the friction coefficient is from 0.2 to 0.45.

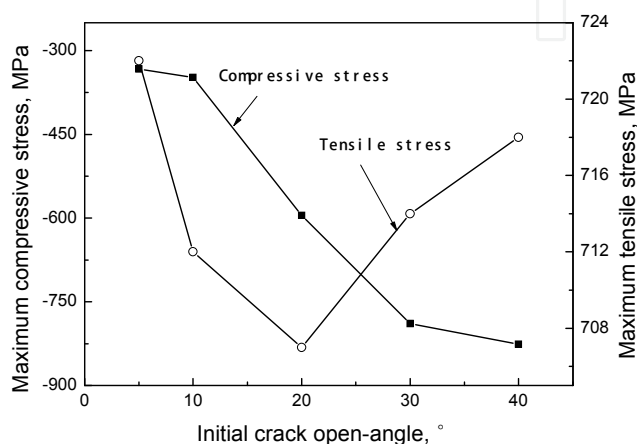


Fig. 5. Maximum compressive and tensile stress at crack tip during rolling for various θ

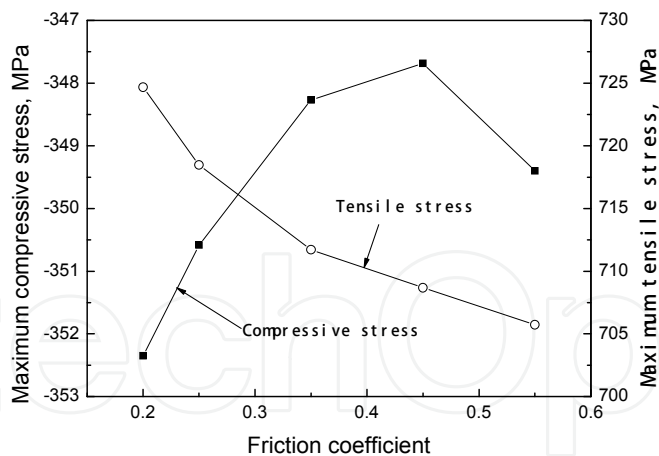


Fig. 6. Maximum compressive and tensile stress at crack tip during rolling for various friction coefficients

Compared the stress value in Figs.4, 5 and 6, the influence of the initial crack open-angle on the maximum compressive stress is the most obvious, whose difference is up to 450 MPa, and the influence of the initial crack height on the maximum tensile stress is the most obvious; the influence of the friction coefficient on the compressive stress is the slightest, and the influence of the initial crack open-angle on the maximum tensile stress is the slightest.

1.2.2 Crack open-angle and height after rolling

Fig. 7 shows the crack open-angle and the crack height after rolling under various the initial crack heights when the initial crack open-angle is 10° and the friction coefficient is 0.35. After rolling, the crack open-angle increases with reducing the initial crack height, and the crack height after rolling is direct ratio to the initial crack height.

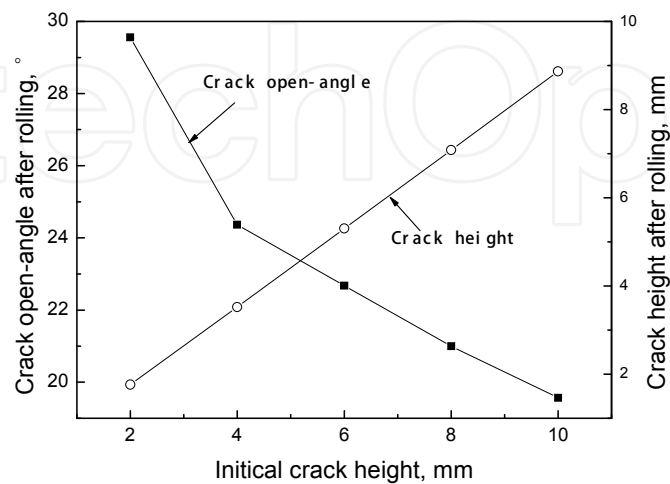


Fig. 7. Crack open-angle and height after rolling for various H_C

Fig. 8 shows the crack open-angle and height after rolling under a variety of initial crack open-angle when the initial crack height is 10 mm and the friction coefficient is 0.35. As the initial crack open-angle increases, the crack height after rolling decreases and the crack open-angle after rolling increases.

Fig. 9 shows the crack open-angle and height after rolling under various friction coefficients when the initial crack open-angle is 10° and the initial crack height is 10 mm. With increasing the friction coefficient, the crack open-angle after rolling increases and the crack height decreases.

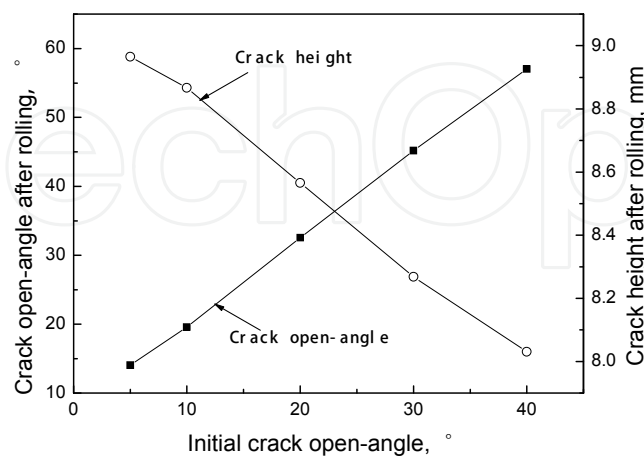


Fig. 8. Crack open-angle and height after rolling for various θ

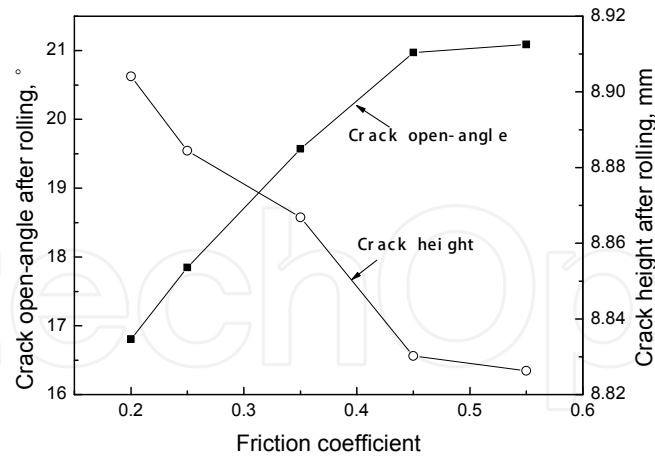


Fig. 9. Crack open-angle and height after rolling for various friction coefficients

1.2.3 Thermal distribution around crack surfaces during rolling

Fig. 10 shows the thermal distribution around the crack when the initial crack height is 10 mm, the initial crack open-angle is 10° and the friction coefficient is 0.35. After rolling, the temperature on crack surface is much less than that in slab matrix. It is obvious that the higher the temperature on crack surface, the more easily the behavior of crack metallurgical healing occurs under the compressive stress. So the thermal distribution around the crack will severely affect the behavior of cracks during rolling.

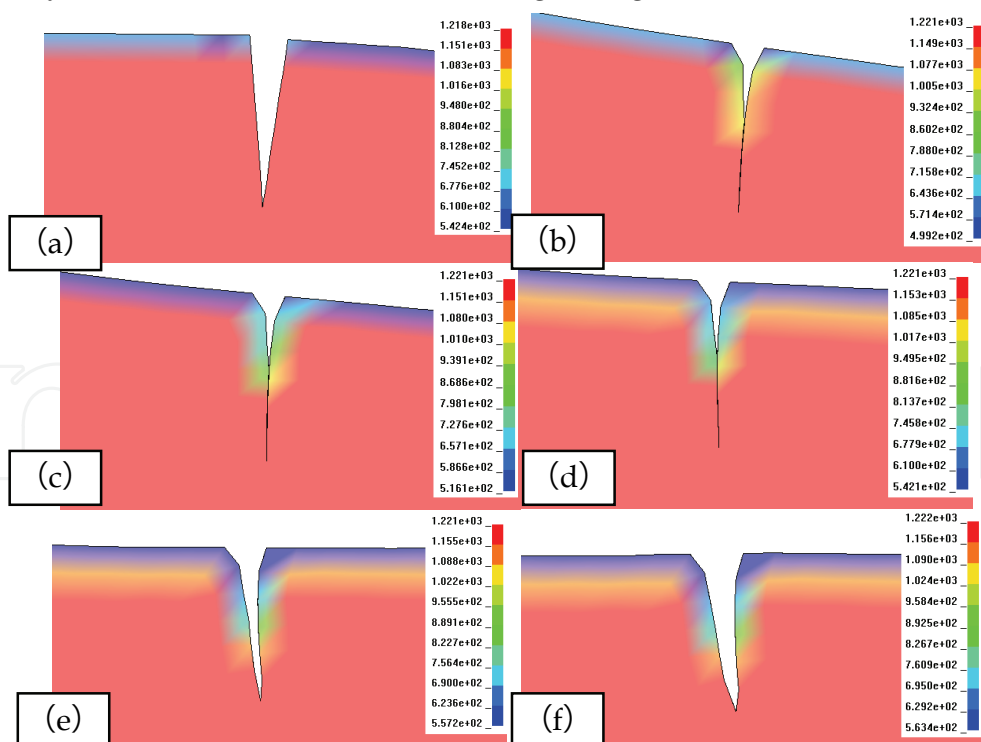


Fig. 10. Thermal distribution around crack at P_1 (a), P_2 (b), P_3 (c), P_4 (d), P_5 (e) and P_6 (f) during rolling ($^\circ\text{C}$)

Fig. 11 shows the temperature variation curve on crack surfaces during rolling under various initial crack heights when the initial crack open-angle is 10° and the friction coefficient is 0.35. In Fig.11 (a), the temperature in P_A changes slightly under various the crack height. As the position approaches to the crack tip, the difference between the temperatures increases. In Fig.11 (b), the temperature in P_B , when the crack height is larger than 8 mm, the temperature changes slightly, and when the crack height is less than 4 mm, the minimum temperature changes slightly and the difference increases as the rolling time increases.

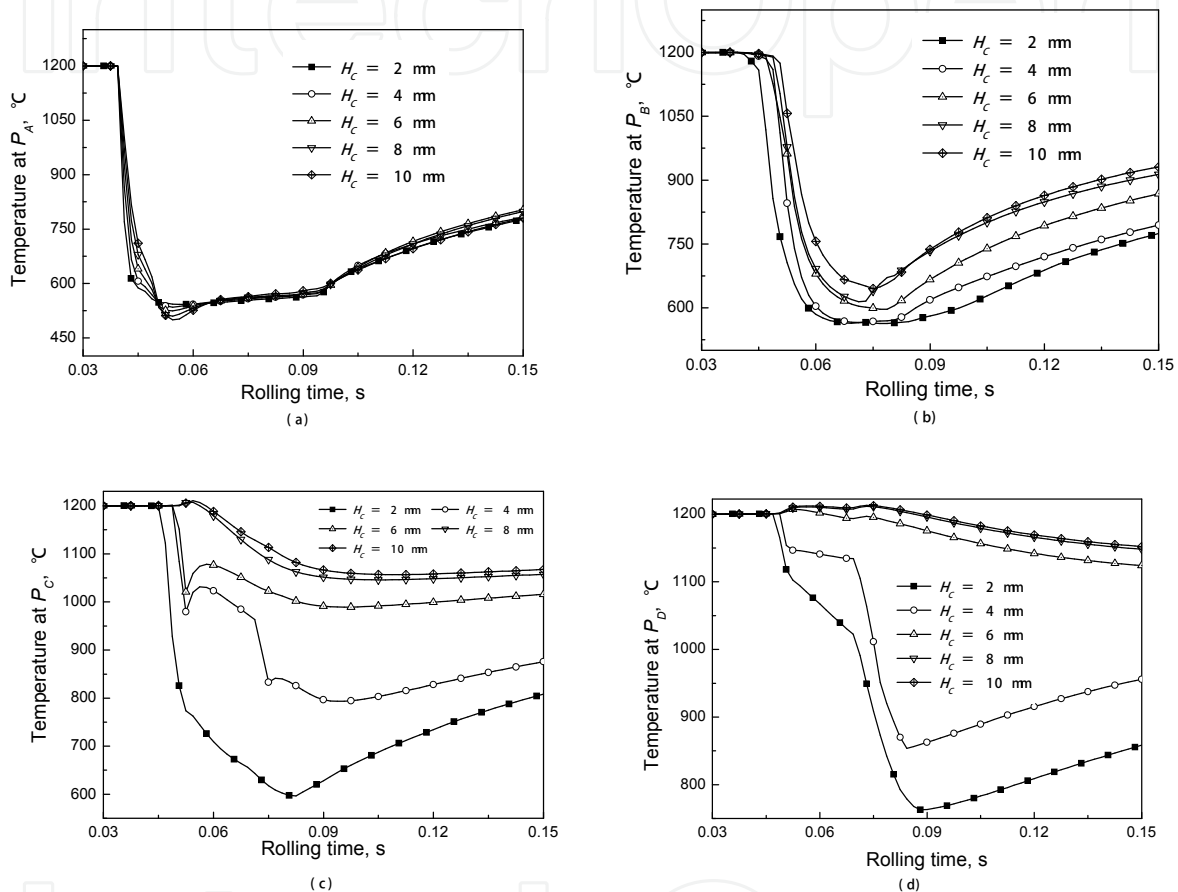


Fig. 11. Temperature at P_A (a), P_B (b), P_C (c) and P_D (d) during rolling for various H_C

In Fig.11(c), when the initial crack height is larger than 4 mm, the temperature increases in the deformation zone, and the temperature directly decreases to minimum temperature in the deformation zone when the initial crack height is 2 mm. In Fig.11 (d), there are two peaks of temperature in the deformation zone when the initial crack height is larger than 6 mm, and the temperature variation is less than 100 °C. When the initial crack height equals to 2 mm, the temperature variation approaches 450 °C.

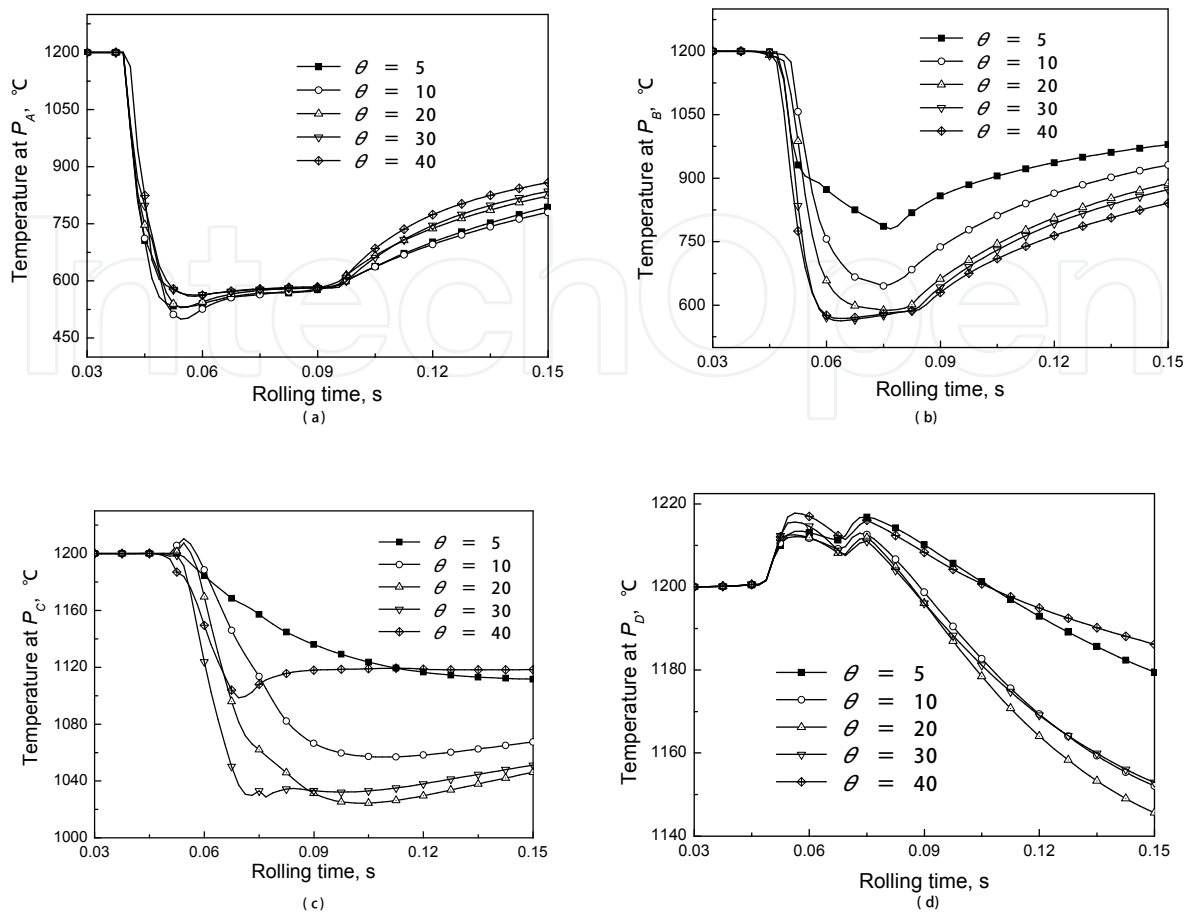


Fig. 12. Temperature at P_A (a), P_B (b), P_C (c) and P_D (d) during rolling for various θ

Fig. 12 shows the temperature variation curve on crack surface under a variety of initial crack open-angles when the initial crack height is 10 mm and the friction coefficient is 0.35. In Fig.12 (a), the temperature varies slightly in the deformation zone, and after rolling, the heating-up speed increases as the crack open-angle increases when it is greater than 10° . In Fig.12 (b), the temperature drop decreases with decreasing the initial crack open-angle. The minimum temperature is about 800°C when the initial crack open-angle is 5° , and the minimum temperature is about 550°C when the initial crack open-angle is 40° , the difference attaches to 250°C . In Fig.12(c), the temperature drop increases with increasing the initial crack open-angle when they are less than 20° , which decreases when they are larger than 20° , that is caused by the plastic work done. In Fig.12 (d), the temperature variation among them is less than 100°C , and they have the same regularity as that in Fig.12(c).

Fig. 13 shows the temperature variation curve on crack surfaces during rolling under various friction coefficients when the initial crack height is 10 mm and the initial crack open-angle is 10° . The temperature on crack surface varies slight during rolling except that the friction coefficient is 0.2. And the temperature rises with increasing the friction coefficient.

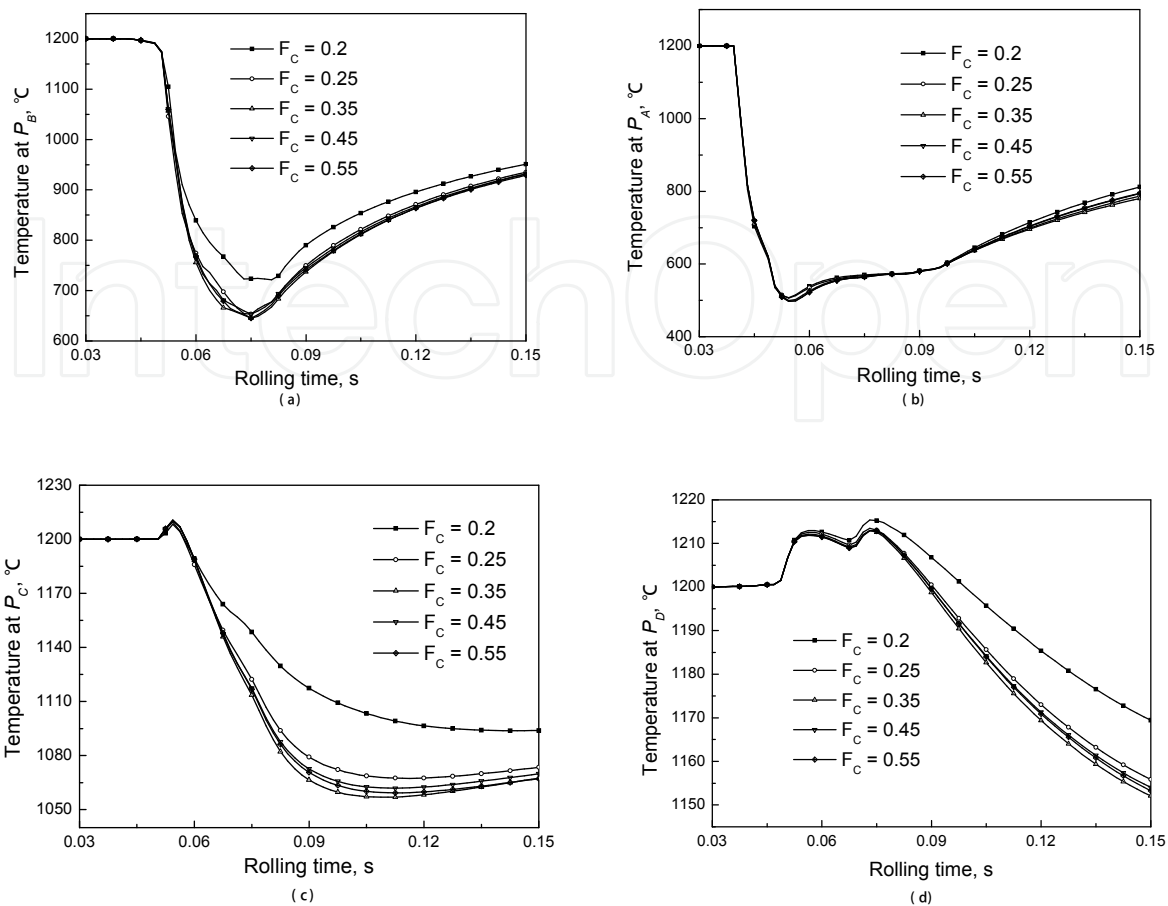


Fig. 13. Temperature at P_A (a), P_B (b), P_C (c) and P_D (d) during rolling for various friction coefficients

From the results above, the cracks close in the bite zone of deformation zone during rolling. The compressive stress appears on the crack surfaces. Then the crack might be healing under the conditions. In the forward slipping zone of deformation zone during rolling, the tensile stress appears around the cracks. When the tensile stress is less than the metallurgical bonding strength, the cracks will not open again, so after a pass, part of cracks heals, then as the rolling passes increase, the cracks gradually close after rolling, as shown in **Fig.14(a)**. When the tensile stress makes part of healing zone open again, the position of P_X might move to the slab surface, after lots of rolling passes, part of cracks heals, and part of cracks becomes the slab surfaces, as shown in **Fig.14 (b)**. When the tensile stress makes the healing part open again, and the crack open-angle is larger than the crack open-angle before rolling, and the crack height decreases after rolling. As the rolling pass increases, the crack surfaces become the slab surface wholly, as shown in **Fig.14(c)**.

The cracks might heal when the temperature is enough high [37, 38], and the influence of thermal and stress distribution around cracks is very important. When the temperature of crack surface is quite low, the metallurgical bonding strength on crack surfaces will decrease severely. As shown in Fig. 11, the temperature distribution on the whole crack surface during rolling is lower than 800 °C when the initial crack height is 2 mm, so the cracks can not heal during rolling. Meanwhile, the crack open-angle after rolling is 29.5° whose initial

crack open-angle is 10° . As the rolling passes increase, the cracks open whole and become part of slab surfaces, as shown in Fig.14 (c). As shown in Fig. 12, the temperature of in P_C and P_D are larger than 1000°C , and the cracks might repair themselves under compressive stress, as shown in Fig.14 (b), even the whole cracks close as shown in Fig.14 (a).

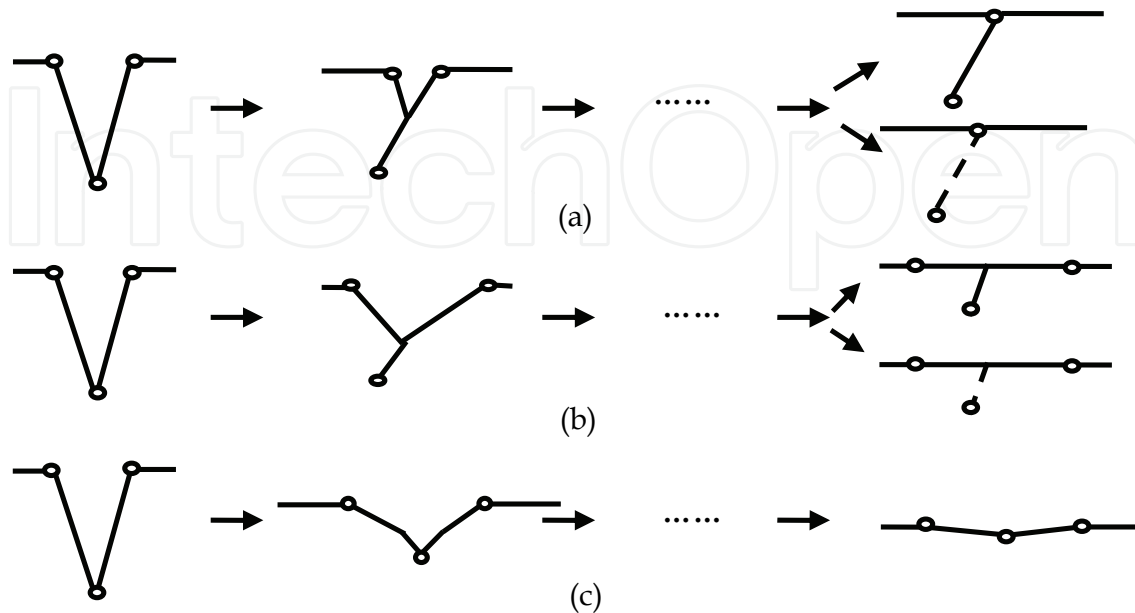


Fig. 14. Schematic of behavior of cracks on slab surface during rolling

2. Evolution of surface cracks on slab corner and edge by 3D FEM

The vertical-horizontal (V-H) rolling has been widely used for adjustment of the slab width for connection between the continuous casting and the finish rolling process. The deformation behavior of slab during rolling affects the quality of rolled steel. The FEM has been widely used for simulation of the behavior of slab during V-H rolling. The behavior of slab during V-H rolling was simulated by Xiong et al with the thermal-mechanical coupled rigid-plastic FEM [39], the thermal distribution and the strain distribution of slab during rolling were obtained, and the unsteady head and tail of slab were analyzed which were in good agreement with those of experimental ones. The three-dimensional rigid plastic/visco-plastic FEM was employed to simulate the behavior of slab during vertical rolling, the slab shape and the rolling force during rolling were obtained that were in good agreement with the experimental ones [40]. The behavior of slab during multi-pass V-H rolling was simulated by the author, and the shape of head and tail of slab during horizontal rolling with different dog-bone shape was also analyzed [41]. In this part, the researches on the evolution of surface cracks on slab corner and edge by 3D FEM were carried out.

2.1 Basic methods of analysis and assumptions

2.1.1 Explicit dynamic FEM

The fundamental equation of explicit dynamic element method [42] is

$$M\ddot{u} + C\dot{u} + F = R \quad (10)$$

Compared with static analysis, the mass matrix and damping matrix are introduced into equilibrium equation of dynamic analysis because of the existence of inertia force and damping force. The final solution equations are ordinary differential equation groups instead of algebraic ones. Generally, the Eq. (10) can be obtained by integrating central difference interpolation, which belongs to immediate integration method. In this method, the discrete velocity and acceleration at t_n can be expressed as:

$$\dot{u}_n = \frac{1}{2\Delta t}(u_{n+1} - u_{n-1}) \quad (11)$$

$$\ddot{u}_n = \frac{1}{\Delta t^2}(u_{n+1} - 2u_n + u_{n-1}) \quad (12)$$

Substituting the Eq.(11) and Eq.(12) into Eq.(10), the discrete-time recurrence equation is obtained as following:

$$u_{n+1} = [M + \frac{\Delta t}{2}C]^{-1}[\Delta t^2(R_n - F_n) + 2Mu_n - (M - \frac{\Delta t}{2}C)u_{n-1}] \quad (13)$$

The central difference method is stable under certain condition that the time step Δt must be lower than Δt_{\min} . Otherwise, the algorithm will be unstable. Generally, according to the Courant-Friedrichs-Levy stability criterion, the critical time step value is:

$$\Delta t_{\min} = \frac{2}{w_{\max}} = \frac{l}{c} \quad (14)$$

For 3D element, the sound velocity in the material is:

$$c = \sqrt{\frac{(1-\nu)E}{(1+\nu)(1-2\nu)\rho}} \quad (15)$$

2.1.2 Contact problem of crack surfaces

In rolling process, the contact problems between the slab and the rolls, between the crack surfaces are the surface to surface problems, which are solved with the penalty function algorithms. The contact stiffness (k) is determined by the Eq. (16)[43].

$$k = \frac{f_s \times A_E^2 \times K}{V_E} \quad (16)$$

Where, f_s is the penalty factor, which equals 0.1 here;

A_E is the area of contact segment;

V_E is the element volumes;

K is the bulk modulus of contacted element. Where $K = \frac{E}{3(1-2\sigma)}$, E is Young's

modulus, and σ is the Poisson's ratio.

2.1.3 Multi-pass rolling process simulation

The updating geometrical method[44] is employed to simulate the multi-pass rolling processes with a single pass rolling process FE model, which is that adding displacements from the previous analysis results and updating the geometry of the finite element model to

the deformed configuration. The updating geometrical process of rolling processes is shown in Fig. 15.

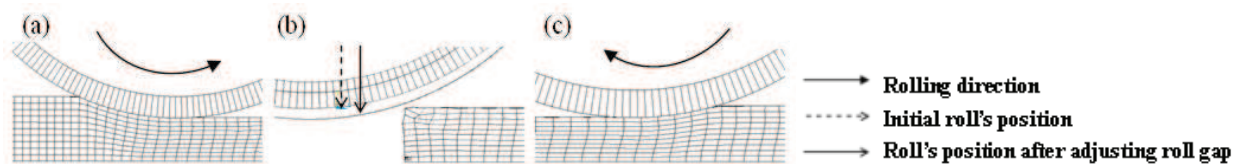


Fig. 15. Updating geometrical process of rolling process

2.1.4 Assumptions

In the research of the closure and growth of crack, there are two assumptions:

- (1) The crack is made up of two surfaces;
- (2) The crack is "V"-shape [29, 30] which exists on slab corner;
- (3) The height of the crack on top surface equals to that on side surface of slab.

2.2 Evolution of corner cracks during rolling

2.2.1 Basic parameters and rolling conditions

The closure and growth of crack during multi-pass V-H rolling process ($V_1-H_1-V_2-H_2-V_3-H_3$) [44] has been simulated. In the simulation, the diameter of horizontal roll is 1150mm. The edger roll of 980mm in diameter separately employs the flat edger roll and the grooved edger roll whose dimensions are shown in Fig.16, where the groove fillet radius R equals to 30, 50, 80 and 110mm. The initial dimension of slab profile is 1200×250mm. The "V"-shape cracks on slab corner are regarded as two surfaces. The crack size (crack height on slab top surface-crack height on slab side surface-crack width) employs 20-20-2 (Fig.17), 15-15-1.5, 10-10-1, 5-5-0.5mm respectively.

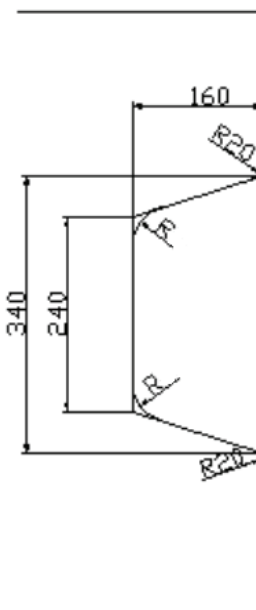


Fig. 16. Dimensions of grooved edger roll

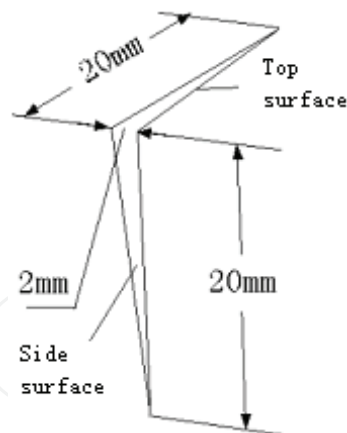


Fig. 17. Dimensions of one kinds of crack with “V”-shape

In this simulation, the rolls are assumed to be rigid and the slab is modeled as bilinear isotropic. The bilinear isotropic model is shown in Eq. (18).

$$\sigma_Y = \sigma_0 + E_P \varepsilon_P^{eff} \quad (18)$$

Where, σ_0 is the initial yield resistance;

ε_P^{eff} is the effective plastic strain;

E_P is the plastic hardening modulus.

The main chemical compositions of slab are (mass %): C 0.18, Si 0.32, Mn 0.82. The yield stress at the high temperature related to the true strain ε , the true strain velocity $\dot{\varepsilon}$, and the deformation temperature T . During this simulation, the initial yield stresses were computed by Eq. (19).

$$\sigma = A \varepsilon^B \dot{\varepsilon}^{C+D} e^{FT} \quad (19)$$

where A, B, C, D, F are constants, as shown in Table 2.

Coefficient	A	B	C	D	F
Value	1715.706	0.17311	0.16952	0.05515	-0.267881

Table 2. Coefficients in the initial yield stress model

In the simulation, the main material parameters are shown in Table 3.

Parameters	Roll	Slab
Young's modulus, GPa	210	117
Poisson's ratio	0.3	0.36
Density, kg/m ³	7850	7850
Plastic hardening modulus, MPa	-	10.1
Initial yield stress, MPa	-	Eq. (19)

Table 3. Basic material parameters in rolling process

During rolling process, the draft of vertical rolling in every pass is 50mm, and the draft of horizontal rolling is 10mm. In this paper, there are 18 kinds of simulation schedules, which are shown in **Table 4**.

Schedule	E-roll shape	R/mm	Crack size /mm	f
1	Flat	—	20-20-2	0.25
2	Flat	—	20-20-2	0.35
3	Flat	—	20-20-2	0.45
4	Flat	—	20-20-2	0.55
5	Groove	50	20-20-2	0.25
6	Groove	50	20-20-2	0.35
7	Groove	50	20-20-2	0.40
8	Groove	50	20-20-2	0.43
9	Groove	50	20-20-2	0.45
10	Groove	50	20-20-2	0.47
11	Groove	50	20-20-2	0.50
12	Groove	50	20-20-2	0.55
13	Groove	50	15-15-1.5	0.35
14	Groove	50	10-10-1	0.35
15	Groove	50	5-5-0.5	0.35
16	Groove	30	20-20-2	0.35
17	Groove	80	20-20-2	0.35
18	Groove	110	20-20-2	0.35

Table 4. Simulation schedules and rolling conditions

2.2.2 Establishment of models

Owing to the symmetry of slab and rolls, 1/4 of slab and rolls were included in the geometric model. According to the parameters mentioned above, the rolling model of the first pass was built. The rolls were considered as rigid because their deformation could be neglected. The whole geometric model was meshed with 8 nodes and hexahedral elements. At the same time, it just refined the elements near the slab margin where the deformation assembled. The nodes on the bottom face of slab were constrained along Y direction, $U_y=0$; and the nodes on the center face of slab were constrained along Z direction, $U_z=0$. The geometrical model and meshing of slab with crack before rolling was shown in **Fig.18**. During simulation, the slab entered the rolls with an initial velocity and exited the rolls under the friction force. The rolling models of the 2nd and the 3rd passes were obtained by updating geometry, changing material attribution, boundary conditions and loads.

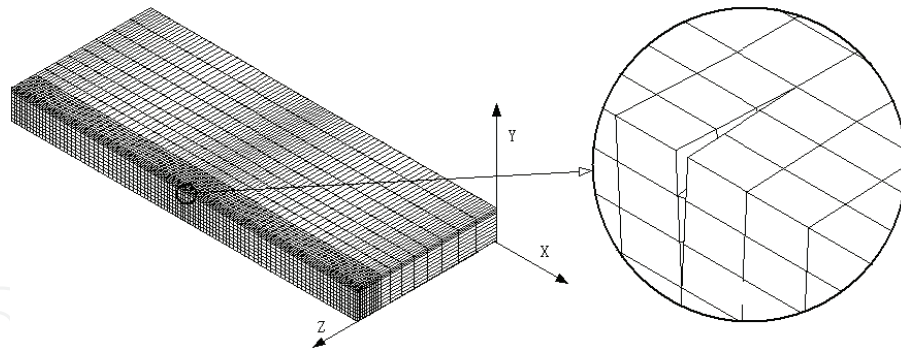


Fig. 18. Geometry and meshing of slab with crack

2.2.3 Results and analysis [45]

The deformation behavior of crack could be realized through the analysis of the change of the crack width during rolling process, which may be used to do the qualitative analysis of the closure and growth of crack. Meanwhile, when the crack closes, two surfaces of the crack will contact each other and appear contact pressure. The contact pressure between crack surfaces may be used to analyze the contact strength for crack surfaces which can be employed to analyze which method is more helpful for the crack closure. However, when the crack is growing or open, the contact pressure will become zero, then, it can't support help for researching. In this paper, the crack width and the contact pressure on crack surfaces at the exit stage of rolling are used to analyze the behavior of transversal crack on slab corner during multi-pass V-H rolling process.

(1) Influence of the friction coefficient on the crack's closure and growth

1> Flat edger roll

When the flat edger roll is used during multi-pass V-H rolling process, after horizontal rolling, the transversal crack on slab corner may close. During following it just analyzes the closure and growth of transversal crack during V_1 - H_1 rolling process. And the simulation schedules 1~4 as shown in **Table 4** are adopted.

<1> Crack width

Fig.19 shows the influence of the friction coefficient on the crack width during V-H rolling process when the flat edger roll is used. In vertical rolling, the influence of friction coefficient on crack width is little, and when the friction coefficient is among 0.25~0.55, the cracks width all are less than 0.25mm. But during horizontal rolling process, the influence of the friction coefficient on crack width is very obvious. When the friction coefficient changes among 0.25~0.35, the cracks close, and when the friction coefficient changes among 0.35~0.55, the final crack width increases gradually with the increasing of the friction coefficient.

<2> Contact pressure

Fig.20 shows the influence of the friction coefficient on the contact pressure on crack surfaces on slab corner during V-H rolling process when the flat edger roll is used. It is very clear that the value of contact pressure in vertical rolling is much larger than that in horizontal rolling. During vertical rolling process, with the changing of friction coefficient, the contact pressure varies among 50~70MPa. And with the increasing of friction coefficient, the contact pressure decreases. During horizontal rolling process, with the increasing of friction coefficient, the contact pressure decreases acutely, from 45MPa to 0MPa, and the crack opens again.

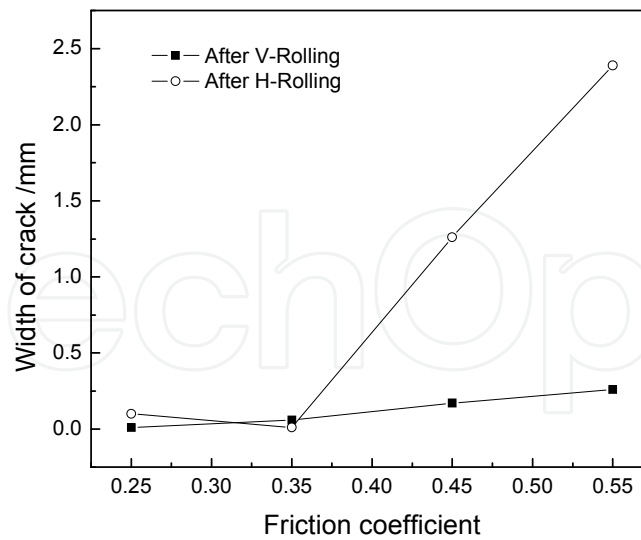


Fig. 19. Influence of the friction coefficient on the crack width after V1 and H1 for flat E-roll

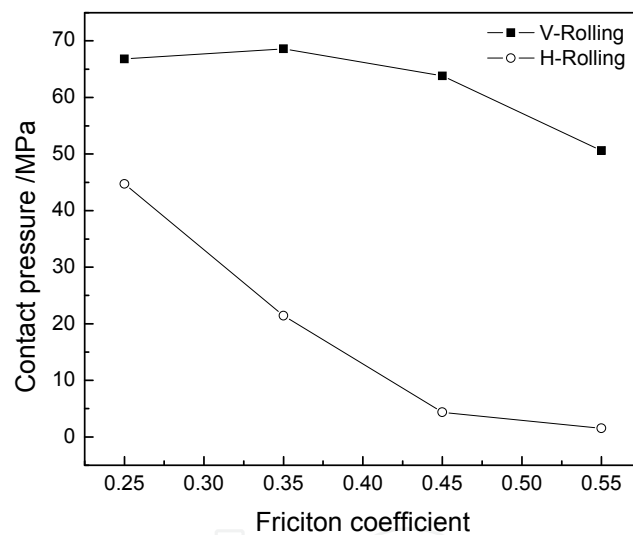


Fig. 20. Influence of the friction coefficient on the contact pressure during V1 and H1 for flat E-roll

2> Grooved edger roll

When the grooved edger roll is used, after horizontal rolling, the crack may be opened again. In the following, the closure and growth of crack is analyzed in the V_1 - H_1 - V_2 - H_2 - V_3 - H_3 rolling process; and the simulation schedules 5~12 as shown in Table 4 are adopted.

<1> Crack width

Fig.21 shows the influence of friction coefficient on crack width during V-H rolling process when the grooved edger roll is used. During vertical rolling process, the cracks close well, but after horizontal rolling process, the cracks all open again. Compared with the crack width when using the flat edger roll, the influence of friction coefficient on crack width is quite small.

<2> Contact pressure

In Fig.22, it could be found that the cracks will open again during horizontal rolling process when using the grooved edger roll. So in the following it just analyzes the influence of friction coefficient on contact pressure during vertical rolling process, as shown in Fig.22. In Fig.22, it could be found that with the increasing of the friction coefficient, the main tendency of contact pressure will decrease during V_1 , V_2 , V_3 rolling process, which isn't good for the closure of crack.

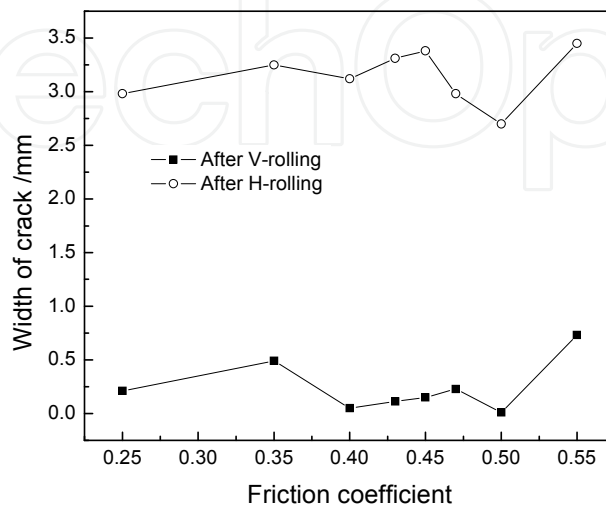


Fig. 21. Influence of the friction coefficient on the crack width after V_1 and H_1 for grooved E-roll

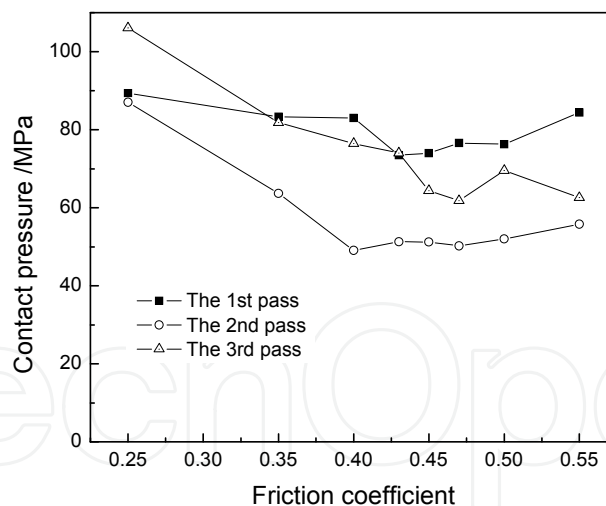


Fig. 22. Influence of the friction coefficient on the contact pressure for grooved E-roll

From the above analysis, it could be known that it is helpful for crack closure to decrease the friction coefficient between the slab and the rolls not only using flat edger roll but also grooved edger roll during multi-pass vertical rolling.

(2) Influence of the initial crack size on the closure and growth of crack

In this following the simulation schedules 6, 13, 14 and 15 are investigated to analyze the influence of crack size on the closure and growth of crack during multi-pass V-H rolling process.

1> Crack width

From above analysis, it is known that the transversal crack on slab corner will close during vertical rolling when the grooved edger roll is used. So in the following it just analyzes the crack width changing after horizontal rolling, which is shown in Fig.23. After H_1 rolling process, when the initial crack size is 20-20-2mm, the crack width is 3.25mm; when the initial crack size is 5-5-0.5mm, the crack width is 1.34mm. And when the crack size is between the former and the latter, the crack width will decrease as the initial crack size decreases after horizontal rolling process.

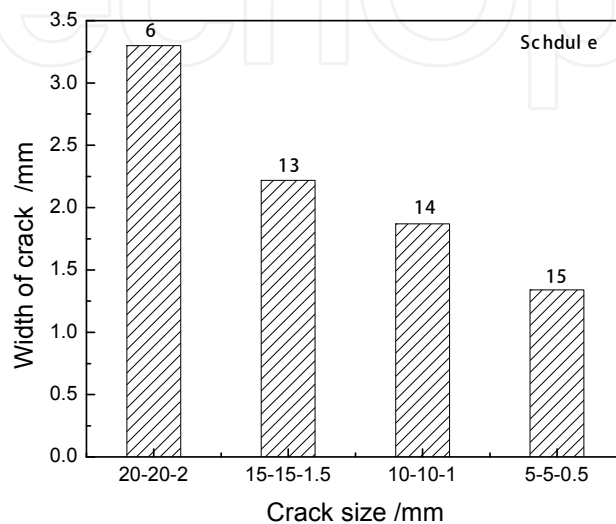


Fig. 23. Influence of the initial crack size on the crack width after H_1 for grooved E-roll and $f=0.35$

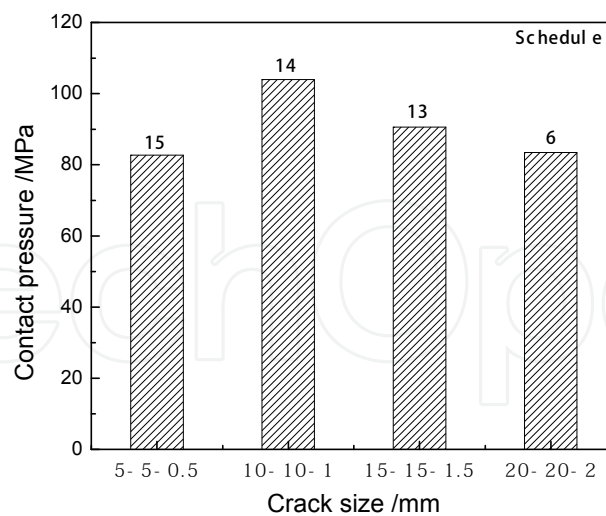


Fig. 24. Influence of the initial crack size on the contact pressure after V_1 for grooved E-roll and $f=0.35$

2> Contact pressure

The contact pressure becomes zero because the crack opens after horizontal rolling process

during V-H rolling process when the grooved edger roll is used. So it just analyzes the contact pressure during V_1 rolling process. Fig.24 shows the influence of initial crack size on the contact pressure of transversal crack on slab corner. In Fig.24, it could be found that the contact pressure of transversal crack decreases as the initial crack size increases when the initial crack size is between 10-10-1mm and 20-20-2mm.

From above analysis it is known that the crack will be easy to close when initial crack size decreases during multi-pass V-H rolling process.

(3) Influence of edger roll shape on the closure and growth of crack

In the below, the multi-pass V-H rolling process (V_1 - H_1 - V_2 - H_2 - V_3 - H_3) were simulated according to the schedules 2 and 6 in Table 4, and the influence of edger roll shape on the closure and growth of crack was analyzed.

1> Crack width

Fig.25 shows the transversal crack width on slab corner after H_1 , H_2 , H_3 rolling process when using the flat edger roll and the grooved edger roll. In the figure, it could be found that the crack closes well for the flat edger roll and the crack opens again for the grooved edger roll. Meanwhile, the crack width decreases with the increasing of rolling pass.

2> Contact pressure

Fig.26 shows the contact pressure of transversal crack on slab corner in each pass both using the flat edger roll and using the grooved edger roll. From which it could be found that the contact pressure is among 70~80MPa during V_1 , V_2 , V_3 rolling process and 0MPa during H_1 , H_2 , H_3 when the grooved edger roll is employed. When employing the flat edger roll, there exists contact pressure in transversal crack on slab corner during V_1 , H_1 , V_2 , H_2 , V_3 , H_3 rolling process, but they all are less than 60MPa.

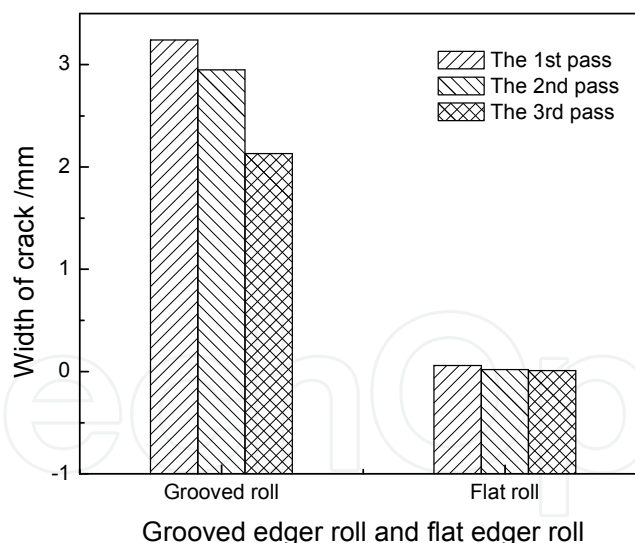


Fig. 25. Influence of the roll shape on crack width

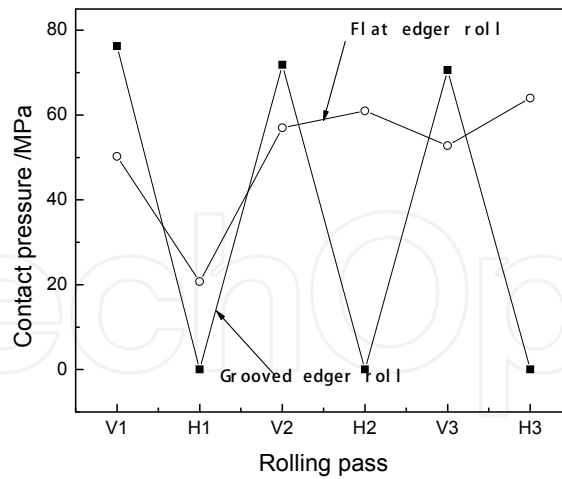


Fig. 26. Influence of the roll shape on contact pressure of crack

From above analysis it could be found that the flat edger roll is more helpful to crack closure than the grooved edger roll when the cracks on some steel grades are hard to heal.

(4) Influence of the groove fillet radius of grooved edger roll on the closure and growth of crack

In the following, the multi-pass V-H rolling process ($V_1, H_1, V_2, H_2, V_3, H_3$) were simulated according to the schedules 6, 16, 17 and 18 in Table 4, and the influence of groove fillet radius on the closure and growth of crack was analyzed.

1> Crack width

Fig.27 shows the width of transversal crack on slab corner under different groove fillet radius of the grooved edger roll. From which it could be known that when the groove fillet radius $R=30\text{mm}$, the crack width is 2.55mm after H_1 rolling process, and it is 2.25mm after H_3 rolling process. With the increasing of R from 50mm to 110mm gradually, the crack width decreases after horizontal rolling process. And what is similar with the Fig.25 is that the crack width decreases as the rolling pass increases.

2> Contact pressure

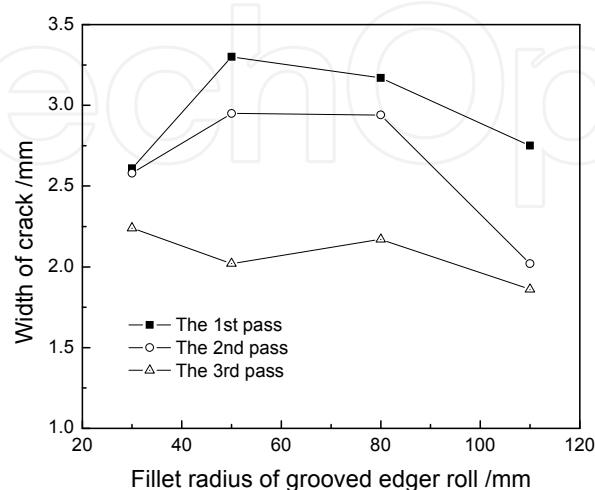


Fig. 27. Influence of the groove fillet radius of the grooved E-roll on crack width

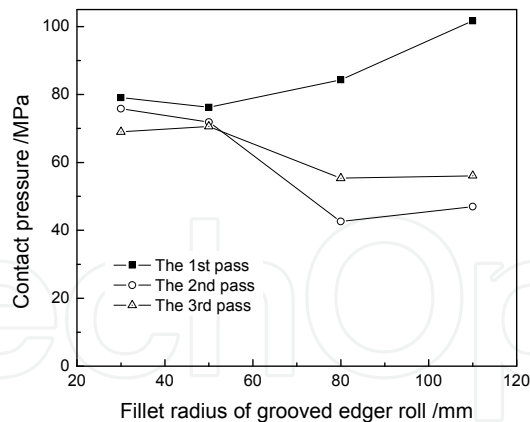


Fig. 28. Influence of the groove fillet radius of the grooved E-roll on the contact pressure

Fig.28 shows the values of contact pressure of transversal crack on slab corner during V_1 , V_2 , V_3 rolling process under different groove fillet radius of grooved edger roll. From the figure, it could be found that the value of contact pressure of transversal crack increases with the groove fillet radius increasing during V_1 rolling process (from 80MPa to 100MPa). But during V_2 and V_3 rolling process, the value of contact pressure of transversal crack decreases with the increasing of the groove fillet radius (from 80MPa to 50MPa). Meantime, if the value of groove fillet radius is relatively small ($R=30\sim 50\text{mm}$), the value of contact pressure is quite stable during vertical rolling process. If the value of groove fillet radius is between 80 and 110mm, the change of the value of contact pressure is larger, from 100MPa to 50MPa. From the above analysis, it could be known that the crack width decreases as the groove fillet radius increases from $R=50$ to $R=110$ mm. Meantime, the value of contact pressure increases during V_1 rolling process and decreases during V_2 and V_3 rolling process as the groove fillet radius increases.

2.2.4 Experimental

(1) Experimental conditions

According to the schedule 1 (as shown in Table 4, the friction coefficient [45] between the lead and the rolls is about 0.2~0.28 in cold rolling), the experiment of the closure and growth of transversal crack during multi-pass V-H rolling process was done in our laboratory.

The $\Phi 300\text{mm}$ mill is adopted in the vertical rolling, and the $\Phi 180\text{mm}$ mill is adopted in the horizontal rolling. The pure lead of slab was used, and the profile of slab is $120\times 25\text{mm}$. The transversal crack with "V"-shape was curved on slab corner. It is shown in **Fig.29**. The height of crack on top surface is 5mm, which on side surface is 5mm, and the width of crack is 0.5mm.

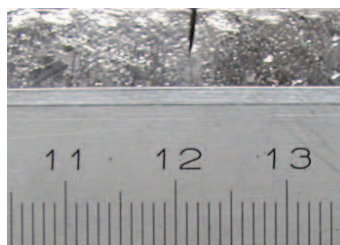


Fig. 29. Experimental sample

During rolling process, according to the rolling schedule V_1 - H_1 - V_2 - H_2 - V_3 - H_3 the experiment is investigated. The rolling velocity is 200mm/s. The draft of vertical rolling in every pass is 5mm, and the draft of horizontal rolling is 1mm.

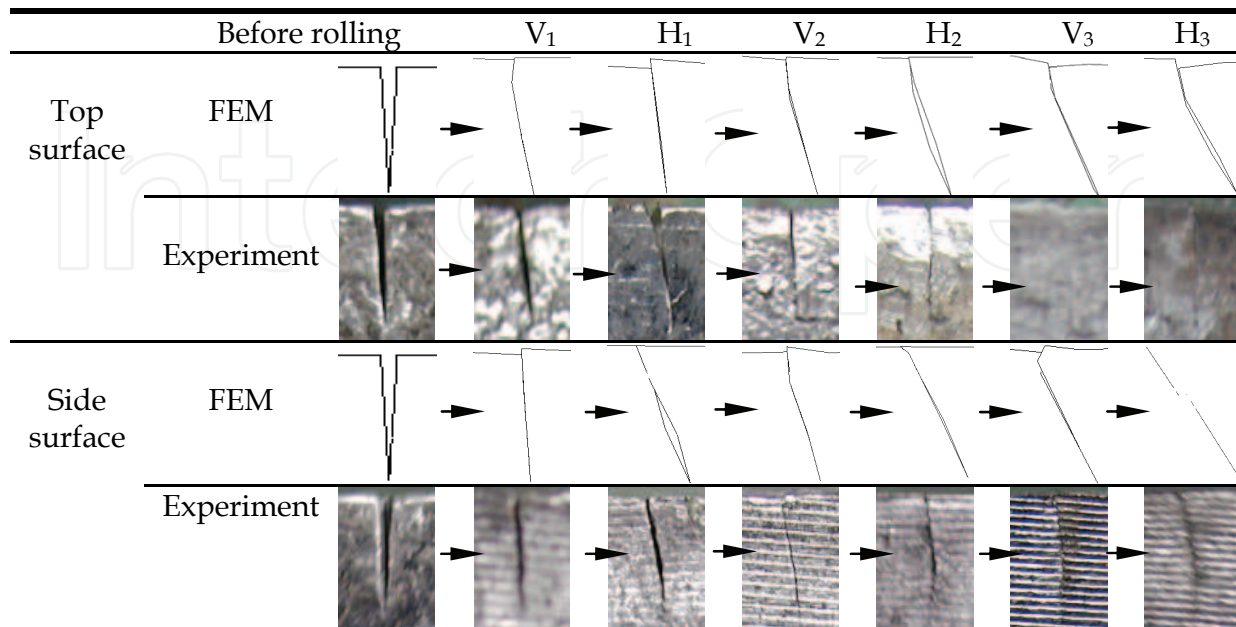


Table 5. Behavior of crack between FEM results and experimental results

(2) Experimental results

The behavior of transversal crack on slab corner during multi-pass V-H rolling process through finite element simulation and experimental simulation is shown in **Table 5**. In the table, the closure and growth from the slab top surface and the slab side surface during every rolling pass could be obvious seen. It is clear that the calculated results have the same tendency of crack behavior with the experiment results using the pure lead.

2.3 Evolution of longitudinal crack on slab edge during rolling

2.3.1 Basic Parameters and Rolling Conditions

In the FE models, the following geometrical parameters are used: the radius of horizontal roll is 1 150 mm; the radius of edger roll is 980 mm employing the flat edger roll and the grooved edger roll respectively, and the fillet radii (R) of grooved edger roll are 30 mm, 50 mm, 80 mm, 110 mm separately, other dimensions of the grooved edger roll are shown in **Fig. 16**. The initial dimensions of slab profile are 250 mm \times 1 200 mm.

The V-shaped (crack width direction) cracks are carved on the upper surface of the slab, which are assumed to be disk-shaped along the crack length direction, as shown in **Fig.30** (X is the rolling direction, Y is the slab thickness direction, Z is the slab width direction). The main parameters of cracks (the crack width, the crack depth and the crack length (w - h - l)) are 2-5-20. In the simulation, it is assumed that the cracks do not weld when the cracks close, and they could be open again.

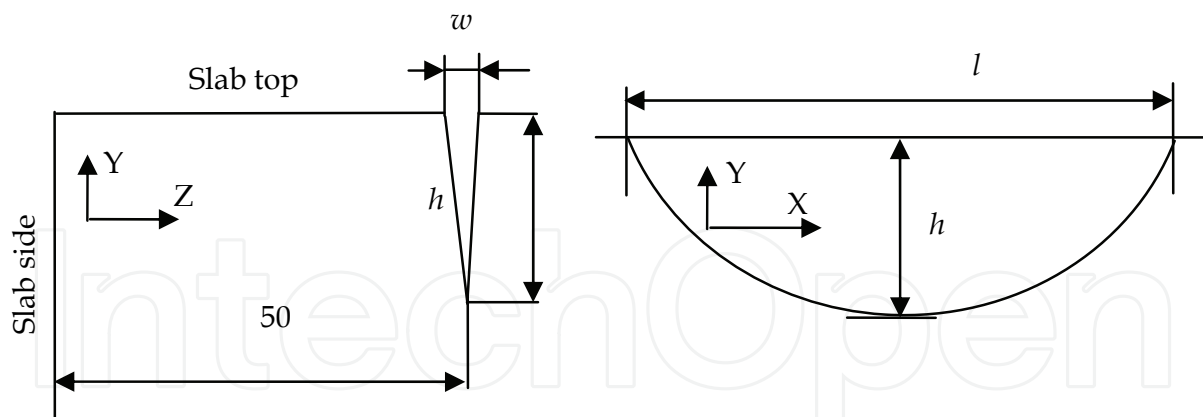


Fig. 30. Crack shape and size

2.3.2 FE Models

Owing to the symmetry of slab and rolls, a quarter of the slab and the rolls were considered in the geometrical model. The V-H rolling models of the first pass were built with the parameters above. The models were meshed with 8-noded hexahedral elements. It just refined the elements near the cracks and the slab margin where the deformation assembled. In rolling process, the edger roll and the horizontal roll rotate with a stable angular velocity, and the slab enters the rolls with an initial velocity and exits under the friction forces. The geometry and meshing of slab with a longitudinal crack on surface in slab edge before rolling is shown in Fig. 31. When building the rolling models of the subsequent passes (V₂-H₃), the step-by-step change in the slab was determined by updating geometry, modifying material attribution, boundary conditions, and loads according to the results of the earlier pass.

During rolling, the draft of vertical rolling is 50 mm each pass, and the outlet thickness after horizontal rolling is 240 mm. The roll rotating speed is 4 m/s. The friction coefficient (F_s) between the slab and the rolls employs three schemes: 0.2, 0.35 and 0.5 respectively.

The nodes on the surface where Y equals 0 are constrained with displacement,

$$U_{Y,Y=0} = 0 \quad (20)$$

The nodes on the surface where Z equals 0 are constrained with displacement,

$$U_{Z,Z=0} = 0 \quad (21)$$

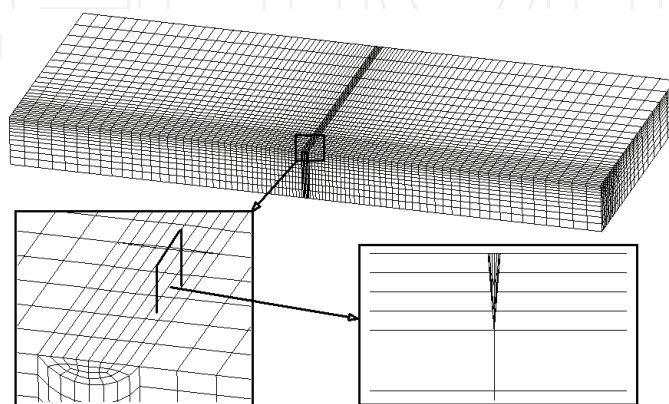


Fig. 31. The geometry and meshing of slab with a longitudinal crack

2.3.3 Results and discussion [46]

Table 6 shows the crack shape from top surface after each pass in multi-pass V-H rolling processes, where R equals 30 mm, 50 mm, 80 mm and 110 mm separately, and F_s equals 0.2, 0.35 and 0.5 separately.

During V-H rolling, the crack closes in vertical rolling process; however, the crack might open again after horizontal rolling process for some kinds of conditions. Meanwhile, with the increase of rolling pass, the crack gradually closes after horizontal rolling process.

When the fillet radii of grooved edger roll are same, the crack width increases as the friction coefficients between the slab and the rolls increase. Similarly, when the friction coefficients are identical, the crack width increases as the fillet radii of grooved edger roll increase.

Fig. 32 shows the influence of fillet radii of grooved edger roll on the crack shape in XY plane when F_s equals 0.35, (a) is after V_1 rolling process, and (b) is after H_1 rolling process. In the figure, the cracks shape in XY plane after rolling is similar to that before rolling process. After vertical rolling, the crack depth increases, meanwhile, which increases with the increase of the fillet radii of grooved edger roll. When R equals 30 mm, the crack depth is around 6 mm, and when R equals 110 mm, the crack depth is around 7.5 mm. Similarly, the crack depth increases as the fillet radii of grooved edger roll increase after the horizontal rolling.

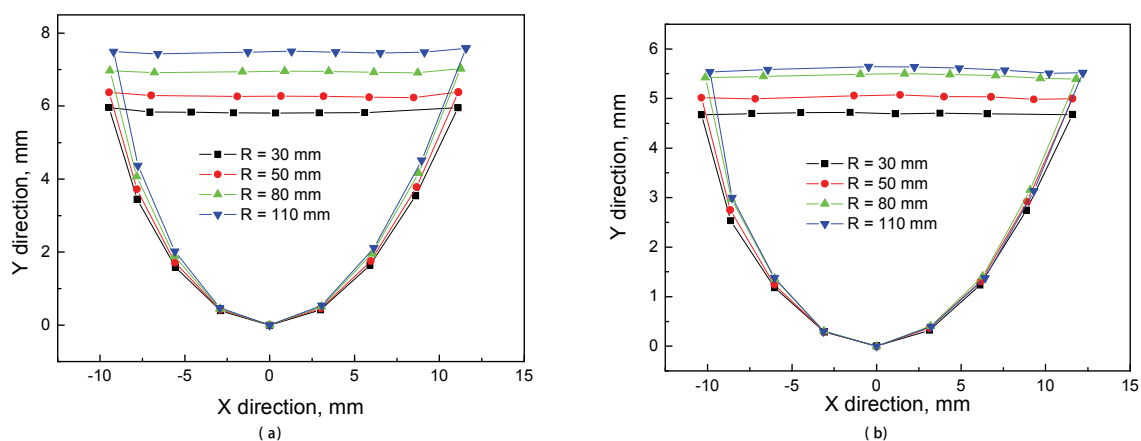


Fig. 32. Crack shape in XY plane for R when F_s equals 0.35 after V_1 rolling (a) and after H_1 rolling (b)

Fig. 33 shows the influence of the friction coefficient on the crack shape in XY plane when R equals 50 mm. The influence of friction coefficient on the crack shape in XY plane is little, and the crack depth increases with the increase of the friction coefficient.

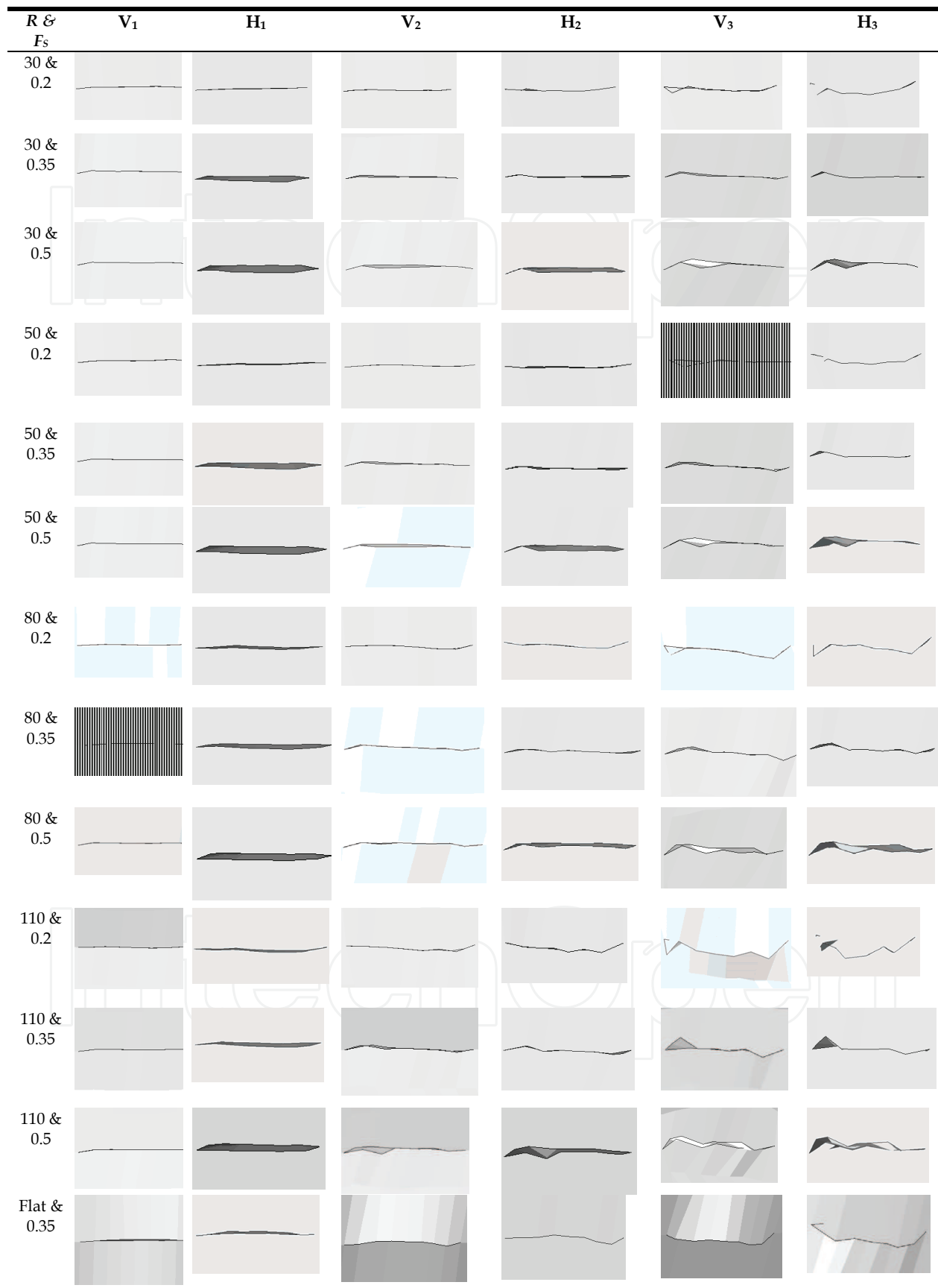


Table 6. Crack shape from top surface in multi-pass V-H rolling processes

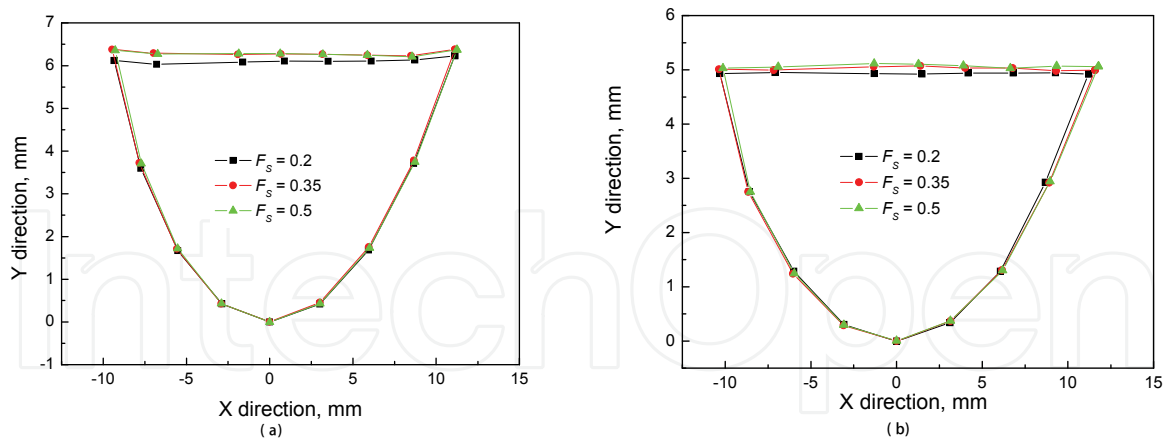


Fig. 33. Crack shape in XY plane for FS when R equals 50 mm after V1 rolling (a) and after H1 rolling (b)

Fig. 34 shows the influence of the fillet radii of grooved edger roll on the crack shape in YZ plane after H_1 rolling process when the F_s equals 0.35. The cracks close well near the crack tip, and they open near slab top surface. Meanwhile, the cracks directions slant to Y direction with a degree. The slant degree increases with the increase of the fillet radii of grooved edger roll during rolling process.

Fig. 35 shows the crack shape in YZ plane after horizontal rolling process when the R equals 50 mm under a variety of the friction coefficients. The cracks close in the zone near crack tip and open near the slab top surface. As the friction coefficient increases, the crack width increases.

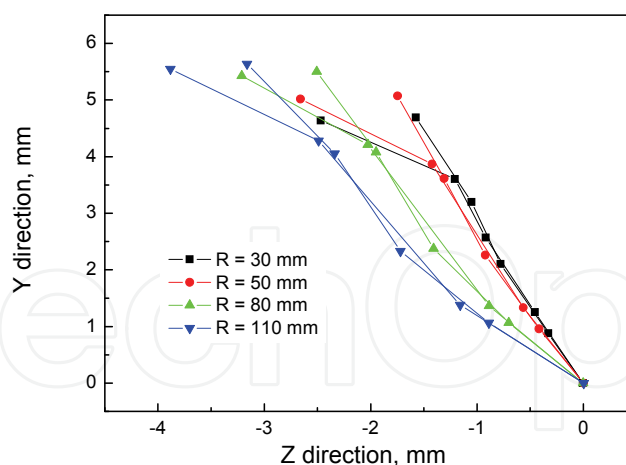


Fig. 34. Crack shape in YZ plane for R when F_s equals 0.35

Analysis of the crack length change regularities in rolling processes. **Fig. 36** shows the influence of fillet radii of grooved edger roll on the crack length elongation ratio (crack length after rolling/ crack length before rolling) in rolling process when the F_s equals 0.35. In V_1 and H_1 rolling process, the crack length elongation ratio increases with the increase of fillet radii, however, the crack length elongation ratio decreases with the increase of fillet

radii in V₂ - H₃ rolling processes. Meanwhile, the crack length elongation ratio when the grooved edger roll is used is larger than that when the flat edger roll is used.

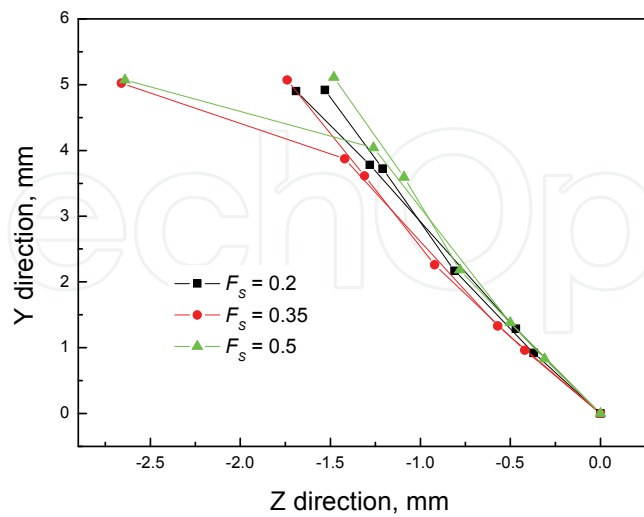


Fig. 35. Crack shape in YZ plane for FS when R equals 50 mm

Fig. 37 shows the influence of the friction coefficient between the slab and the rolls on the crack length elongation ratio when the fillet radius equals 50 mm. The crack length after rolling increases as the friction coefficient increases.

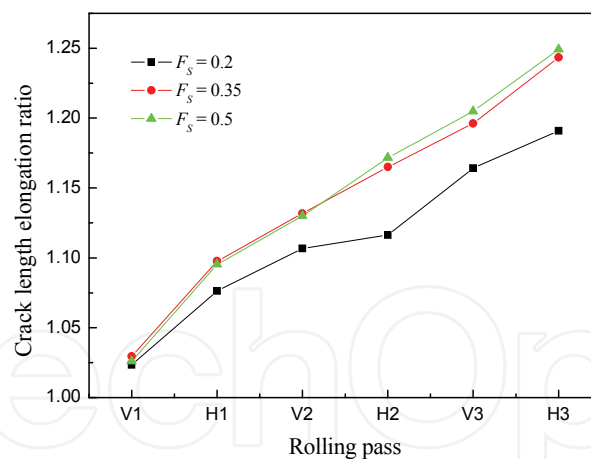


Fig. 36. Crack length elongation ratio for edger roll shape when FS equals 0.35

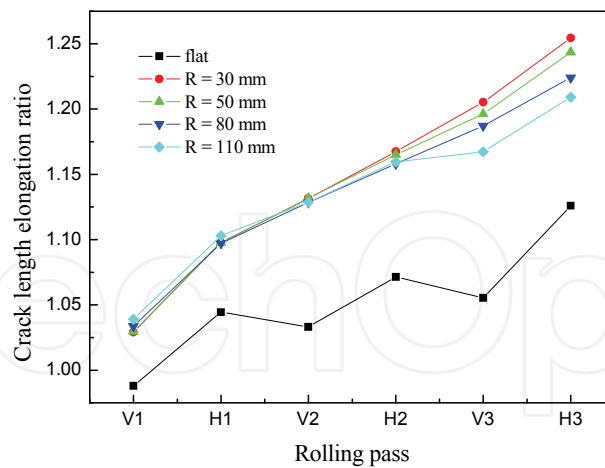


Fig. 37. Crack length elongation ratio for friction coefficient when R equals 50 mm

2.3.4 Experimental

Pure lead is often used for simulation of the slab deformation during hot rolling, because the mechanical characteristics of the pure lead at room temperature are similar to that of steel at high temperature. Meanwhile, the pure lead is also used to simulate the behavior of defects in steel hot deformation process.

In order to validate the calculated results, experiments of the closure and growth of longitudinal cracks on surface of slab edge in multi-pass V-H rolling processes were investigated in laboratory with the pure lead. The vertical rolling employs the $\Phi 300$ mm mill with grooved roll whose fillet radius is 11 mm; the horizontal rolling employs the $\Phi 180$ mm mill. The dimensions of slab profile are 25 mm \times 120 mm, and a V-shaped longitudinal crack is carved on the top surface in slab edge, the crack width is 0.6 mm, the crack depth is 1.5 mm, and the crack length is 6 mm. The rolling speed is 200 mm/s. In rolling process, according to the V₁-H₁-V₂-H₂-V₃-H₃ rolling schedule, the draft in vertical rolling is 5 mm, and the draft in horizontal rolling is 1 mm.

Table 7 shows the crack shapes after each pass between the calculated results and the experimental results (the friction coefficient between the pure lead and the steel is around 0.2). From the results, the calculated results have the similar deformation regularities with the experimental results. After the V₁ pass, the cracks close well, however, after the H₁ pass, the crack opens a little. In the subsequent passes, the crack gradually closes, after the V₃ pass, the crack nearly closes well.

Fig. 38 shows the crack length elongation ratio between the calculated results and the experimental results. In the figure, the differences between the experimental results and the calculated results are small. In the V₁~H₂ passes, the experimental results are around the calculated results; and in the V₃ and H₃ passes, the experimental results are few larger than the calculated results. About the differences between the experimental ones and the calculated ones, the main reason is the different roll radii between the experiment and the FE simulation. Meanwhile, the influence of the thermal distribution in slab during rolling on the behavior of cracks need to be further studied in future.

Rolling pass	Vertical rolling process		Horizontal rolling process	
	Calculated results	Experimental results	Calculated results	Experimental results
1				
2				
3				

Table 7. Compared the calculated results with the experimental ones of the crack shape from top surface

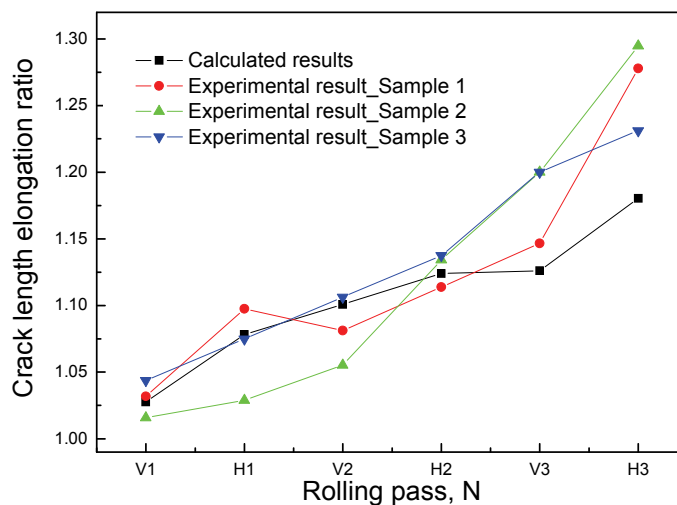


Fig. 38. Compared the calculated results with the experimental ones of the crack length elongation ratio

3. Evolution of internal cracks at slab edge by 3D FEM

The internal cracks might appear in slabs during continuous casting for the thermal stress, friction force, mechanical force, etc [47]. During hot rolling, the cracks might close, even heal. However, they might propagate for the concentrated force or other reasons. So analysis of the closure and growth of cracks during rolling is significant for improvement of the slab quality.

3.1 Parameters and boundary conditions

The diameter of horizontal roll is 1 150 mm. The diameter of grooved vertical roll is 980 mm, and other dimensions are shown in Fig. 16, where the R is 50 mm (30, 80, 110 mm used in

analysis of the behavior of cracks under various the fillet radius of grooved vertical roll). The dimension of slab profile before rolling is 1 200×250 mm. The cracks are assumed to be disk-shape cracks. **Fig.39** shows the schematic drawing of cracks shape, position, and size, where, X is rolling direction, Y is slab thickness direction, Z is slab width direction. In this simulation, the crack width and the crack height ($w \times h$) is 0.1×1 mm (0.2×2, 0.3×3, 0.4×4 mm used for analysis of the behavior of cracks under various crack size). And the crack position ($W \times H$) is 62.5×25 mm (0×25, 31.5×25, 93.75×25 mm and 62.5×125, 62.5×100, 62.5×75, 62.5×50 mm used in analysis of the behavior of cracks under various crack positions). During rolling, the draft in vertical rolling is 50 mm, and the draft in horizontal rolling is 10 mm (15, 20, 25 mm used in analysis of the behavior of cracks under various the draft in horizontal rolling). The friction coefficient between the slab and the rolls is 0.35. And the rotating speed of rolls is 4 m/s.

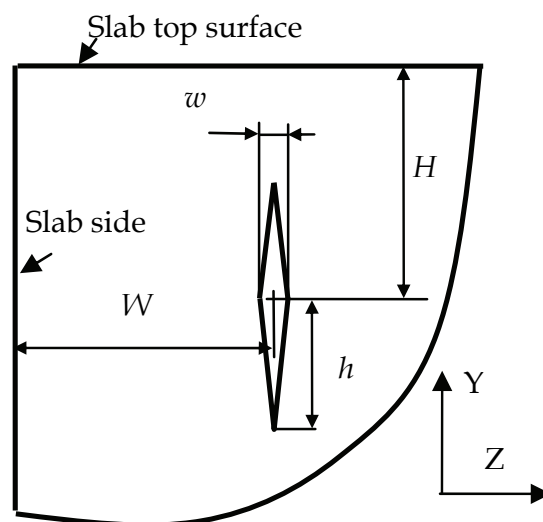


Fig. 39. Crack shape, size, position

The rigid material model is employed for rolls and the bilinear isotropic hardening material model for slab. In the simulation, the initial deformation resistance is calculated by Eq. 19. The main materials parameters are shown in **Table 3**.

3.2. FE models

Owing to the symmetry distribution of the rolls and slab, a quarter of rolling parts is employed. Because the crack size is much smaller than the slab size, an inlaid model is used. According to the parameters above, the FE model of V-H rolling process has been established. The whole model is discretized by the 8-noded hexahedral elements. The nodes on the symmetry plane of slab thickness are constrained, $U_Y = 0$; the nodes on the symmetry plane of slab width are constrained, $U_Z = 0$. During rolling process, the slab enters rolls with an initial speed and exits rolls under the action of friction force. The geometry and meshing of slab with an internal-longitudinal crack is shown in **Fig. 40**.

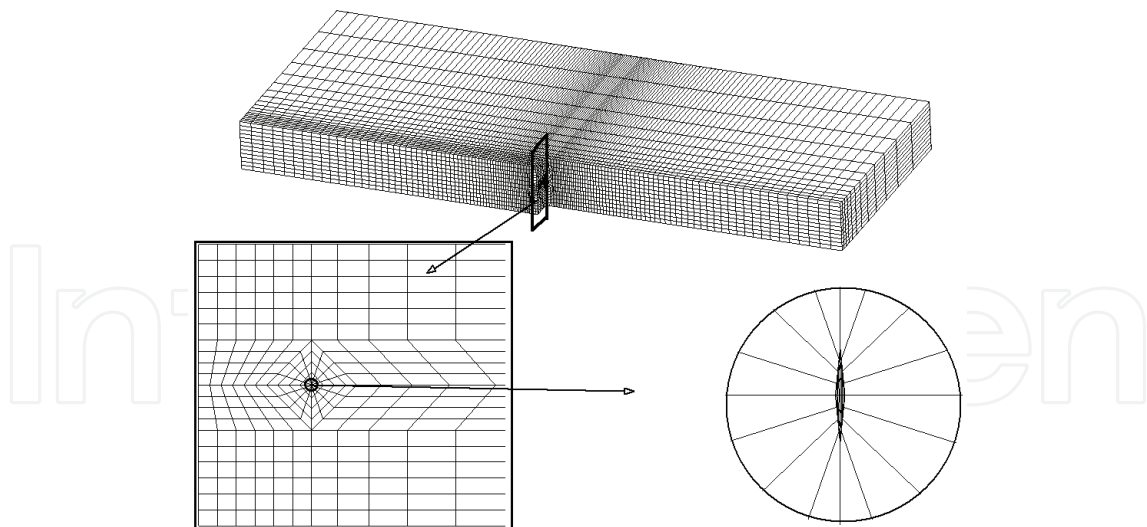


Fig. 40. Geometry and meshing of slab with an internal-longitudinal crack

3.3 Results and discussion [48]

Fig. 41 shows the crack shapes during rolling, where (a)~(d) are the crack shape during vertical rolling, and (e)~(f) during horizontal rolling. During vertical rolling, the crack gradually closes. As shown in Fig. 41 (d), the crack closes well. But during horizontal rolling, the crack gradually grows. As shown in Fig. 41 (g), the crack clearly appears in slab. Compared the crack size in Fig. 41 (g) with that in Fig.41 (a), the former is much less than the latter.

It is easy to understand that the crack surfaces will contact each other when the crack closes, and then an action force which is named the contact pressure will appear on crack surfaces. **Fig. 42** shows the curve of contact pressure on crack surfaces (next just says contact pressure) during rolling process. The contact pressure during vertical rolling is larger than that during horizontal rolling. In the bite zone of vertical rolling, the contact pressure gradually increases from 0 to 220 MPa, but which gradually decreases to 80 MPa in the exit zone of vertical rolling. In horizontal rolling, the contact pressure shapely decreases to 40 MPa, and exit about 20 MPa. In the below, the maximum value of contact pressure during vertical rolling and horizontal rolling are employed to analyze the influencing factors on the behavior of cracks.

Fig. 43 shows the maximum value of contact pressure during V-H rolling under a variety of fillet radii of grooved vertical roll. With increase of fillet radii, the contact pressure gradually increases from 110 MPa to 260 MPa during vertical rolling, but which gradually decreases from 50 MPa to 30 MPa during horizontal rolling. So the crack will be easily healed as the fillet radius increases.

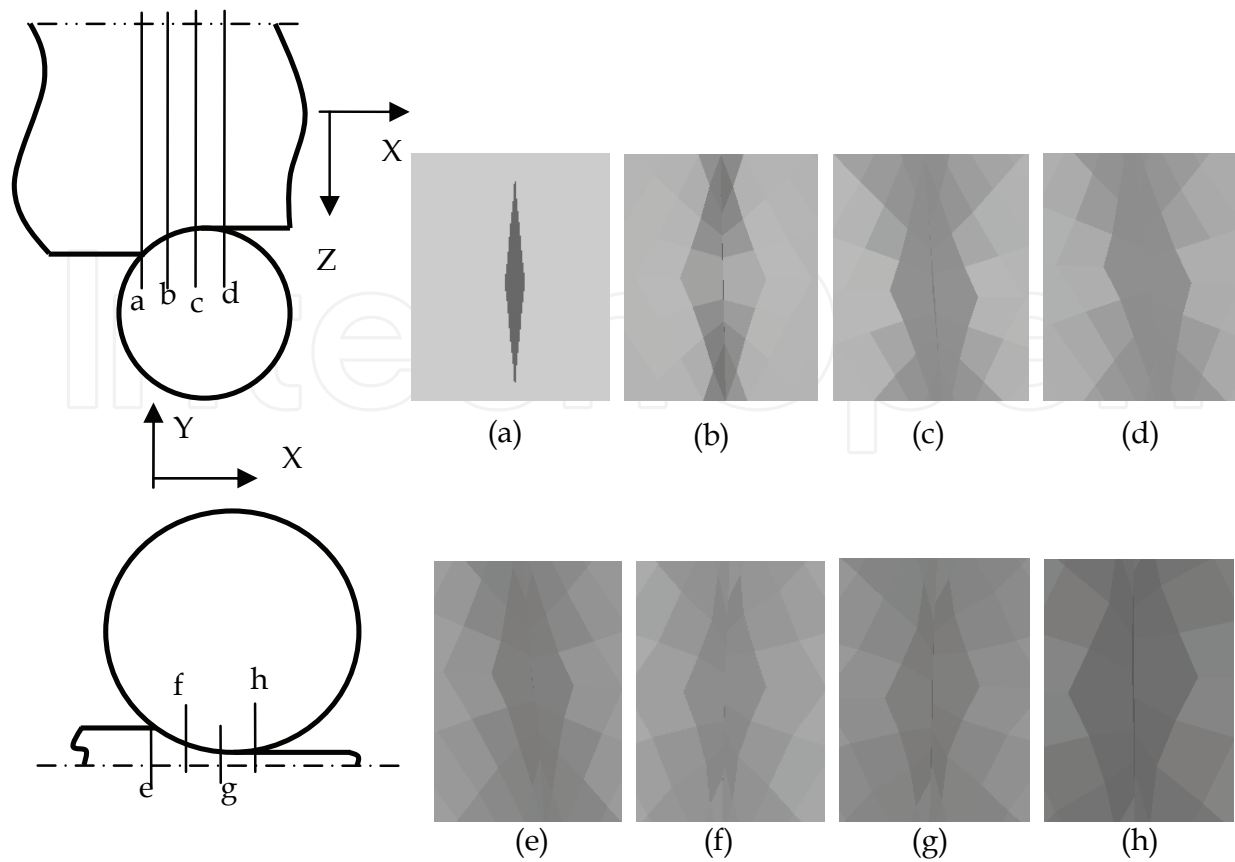


Fig. 41. Crack shape during V-H rolling

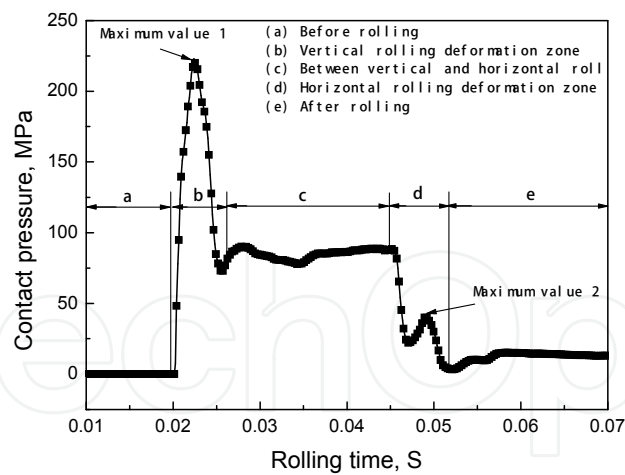


Fig. 42. Contact pressure on crack surfaces during V-H rolling

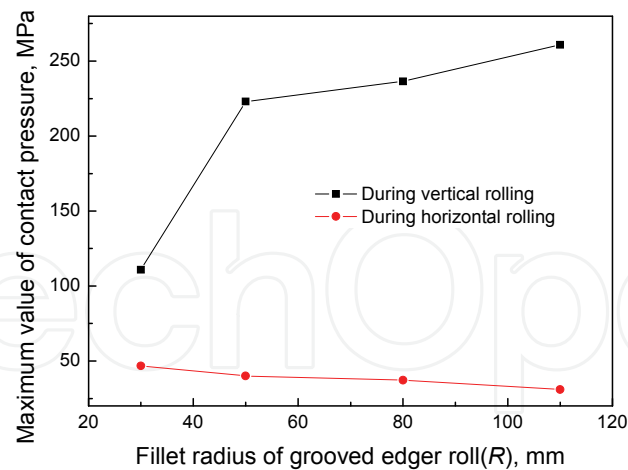


Fig. 43. Maximum value of contact pressure for various fillet radius of grooved vertical roll

Fig. 44 shows the maximum value of contact pressure during rolling under a variety of distance away slab central line along thickness direction (125-H). During vertical rolling, with increases of the distance away slab central line along thickness direction from 0 to 63 mm, the contact pressure increases, but the contact pressure decreases from 63 to 93 mm. During horizontal rolling, the contact pressure gradually increases as the distance increases.

Fig. 45 shows the maximum value of contact pressure during rolling under a variety of distance away slab central line along width direction (600-W). During vertical rolling, with increases of distance, the contact pressure increases from 0 to 221 MPa. During horizontal rolling, the contact pressure increases when the distance is between 450 and 500 mm but decreases when the distance away slab central line along width direction is between 500 and 575 mm.

Fig. 46 shows the maximum value of contact pressure during rolling under a variety of crack sizes. During rolling, when the crack width is less than 0.2 mm, the contact pressure changes slightly. However, with increases of crack size, the contact pressure sharply decreases. When the crack width is larger than 0.3 mm, the crack can close well under this rolling condition.

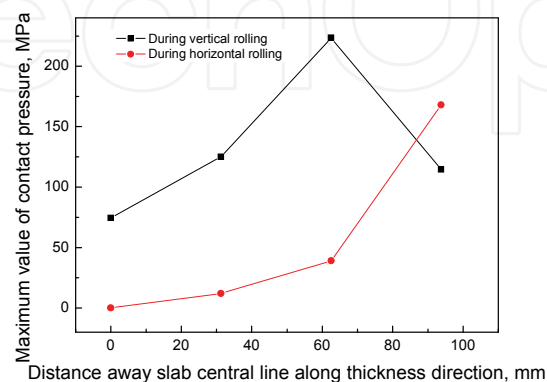


Fig. 44. Maximum value of contact pressure for various distance away slab central line along thickness direction

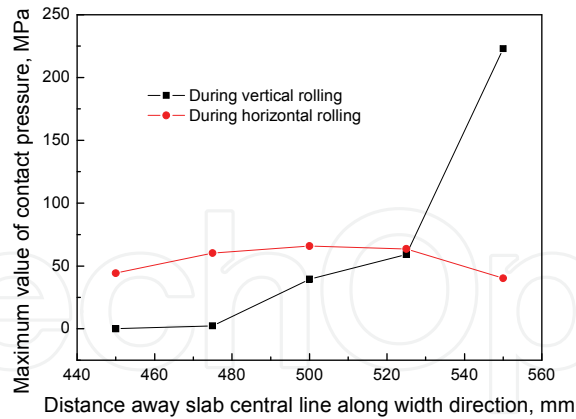


Fig. 45. Maximum value of contact pressure for various distance away slab central line along width direction

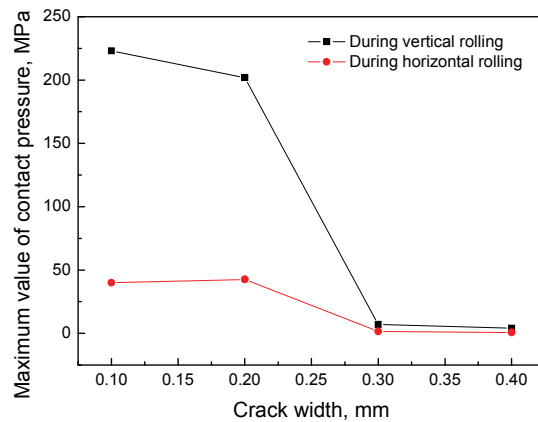


Fig. 46. Maximum value of contact pressure for various crack sizes

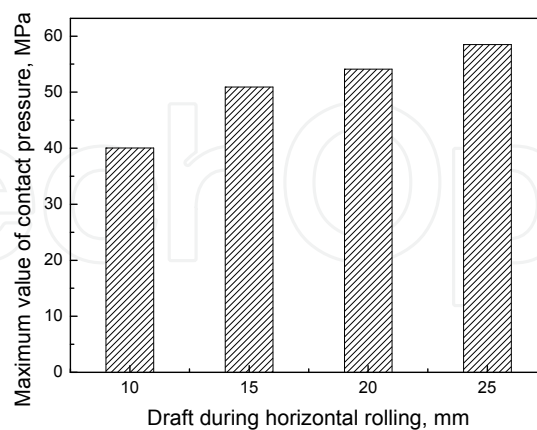


Fig. 47. Maximum value of contact pressure for various drafts during horizontal rolling

Fig. 47 shows the maximum value of contact pressure during rolling under a variety of draft in horizontal rolling process. During rolling, with increases of the draft, the contact pressure increases.

During hot rolling, the rolling temperature is high which generally is about 800~1200 °C. At this time, the ions near the crack surfaces are very activity. Meanwhile, there are many influencing factor which might make the cracks heal, such as power supplement, matter supplement. So the cracks might heal during rolling. **Fig. 48 [49]** shows the condition of crack healing under various slab reductions. As shown in the figure, the crack size decreases clearly with increase of slab reduction ratio. And when the rolling conditions are certain, the contact pressure will decrease as the crack size increases, as shown in Fig. 46.

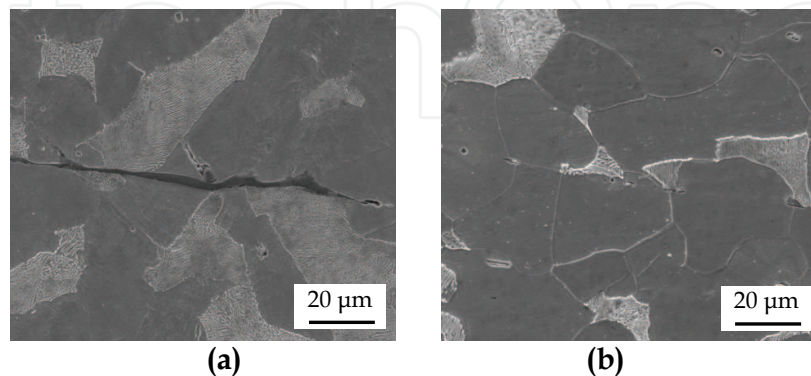


Fig. 48. Crack shape under 5%(a) and 50% (b) slab reductions during hot rolling[48]

It is easy to understand that the compression stress in slab increases with increase of slab reduction ratio, which means that the contact pressure will increase. So as the contact pressure increases, the cracks will be easier to heal. From the results above, we know the contact pressure during vertical rolling is much larger than that during horizontal rolling. So when the internal-longitudinal cracks appear in slab, it is significant to control the slab vertical rolling. As the fillet radii increase, the equivalent reduction ratio of slab increases, so the contact pressure increases. Meanwhile, the contact pressure also increases with increase of reduction ratio of slab during horizontal rolling, as shown in Fig. 47.

Fig. 49 [50] shows the strain distribution during rolling process. During vertical rolling, the deformation of slab mainly assembled near slab edge, so the contact pressure decreases when cracks approaching the slab central line along slab width direction. Meanwhile, the strain also decreases when approaching the slab central line along slab thickness direction, so do the contact pressure, as shown in Figs. 44 and 45.

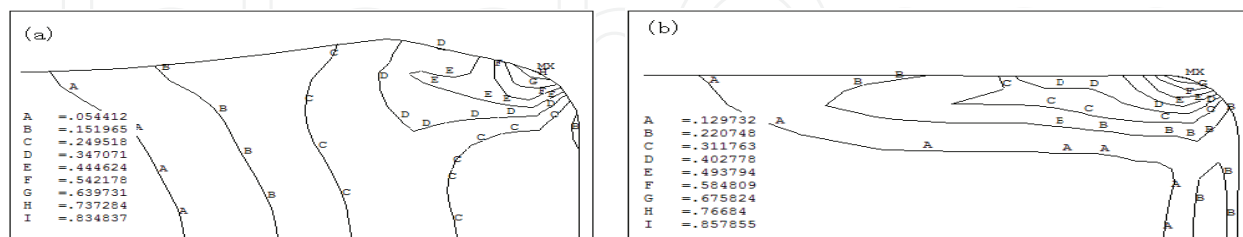


Fig. 49. Strain distribution after vertical (a) and horizontal (b) rolling

4. Evolution of inclusions in strip during rolling by FEM

The non-metallic inclusions inevitably exist in steel strips for the deoxygenation, etc, which is still one of the most important topics during continuous casting although their quantity, size, shape, distribution and composition are controlled at a lower level [51]. The chemical compositions of

non-metallic inclusions in type 304 stainless steel strips mainly are the oxide of aluminum, silicon, chromium, manganese, etc [52]. The distribution and the size of inclusions severely affect the quality of strips. Analysis of the deformation of non-metallic inclusions in rolling process is significant for improvement of the strip quality.

The FEM has been used for analyzing the deformation of inclusions in a slab during rolling. A rigid-viscoplastic 2D FE code was developed to analyze the shape of inclusions during rolling along rolling direction of oxidized inclusions [53] and MnS inclusions [54] in flat rolling process under different rolling temperature, friction and rolling schedules. The start of void deformation close to a hypothetical single circle macro-inclusion in the hot rolling of steel slabs which was affected by the reduction, roll radius and inclusion position was simulated through the FE-code LS-Dyna3D [55]. It pointed out that the large roll radii should be chosen for preventing void initiation, heavy draughts resulting in large contact lengths are favorable and inclusion close to the surface are less dangerous than those in the centre of the slab. The void generation and development around a rigid circle inclusion simulated by FEM [56] showed that the void length in front of inclusion was larger than that in rear of inclusion under different rolling conditions. The behavior of short cracks between the inclusions and the matrix under rolling contact fatigue load was simulated by Melander [57] who analyzed the effects of the inclusion shape on the behavior of cracks. In this chapter, the application of FEM in simulation of evolution of cracks and inclusions in rolled steel during rolling was carried out. In this part, the researches on the evolution of inclusions during flat rolling were carried out.

4.1 Evolution of inclusions combined with matrix

4.1.1 Basic parameters and rolling conditions

Fig. 50 shows the schematic drawing of rolling strip with a spherical inclusion, where X is rolling direction, Y is the strip thickness direction, and Z is the strip width direction.

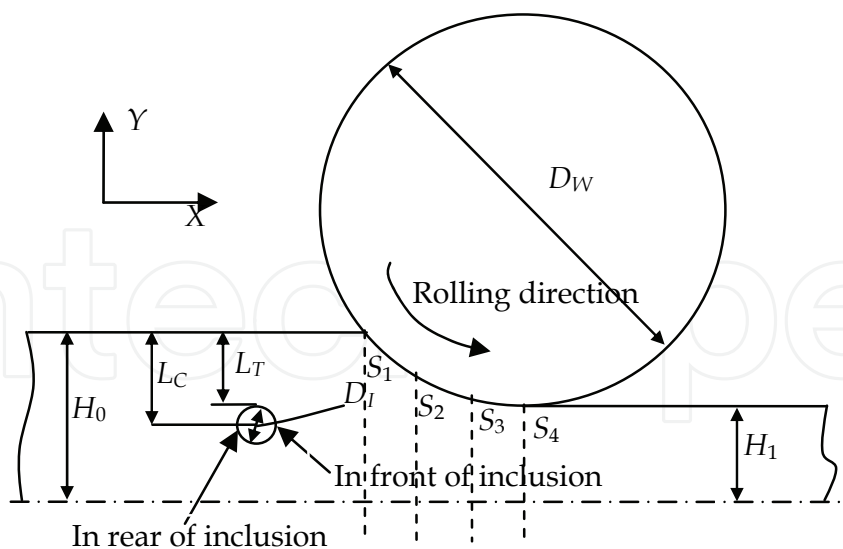


Fig. 50. Schematic drawing of rolling strip with a spherical inclusion

In the simulation, the work roll diameter (D_W) is 400 mm. The diameters of inclusion (D_i) are 10, 20, 30, 40, 50 μm respectively which are assumed to be spherical and in the position of $1/8$, $1/4$, $3/8$ and $1/2$ of strip thickness ($L_C/(2H_0)$). A part of strip is employed whose width

is 30 mm for saving computing time. The friction coefficient between the strip and the roll is 0.15. And the rolling schedule is shown in **Table 8**.

Rolling pass, N	1	2	3
Strip thickness before rolling ($2H_0$), mm	3.0	2.0	1.4
Strip thickness after rolling ($2H_1$), mm	2.0	1.4	1.0

Table 8. Rolling schedule

During rolling, the strip matrix is the type 304 stainless steel, and the inclusion is assumed to be Al_2O_3 (As shown in **Fig. 51**). The main material parameters of rolls, strip matrix [58] and inclusion [59] used in FE models are shown in **Table 9**. The deformation resistance of strip in the i th pass is calculated by Eq. (20).

$$\sigma = C[0.001 + \ln(\frac{h_i}{H_0})]^n \quad (20)$$

where, C is the constant related to the strip temperature, h_i is the strip thickness in the i th pass, H_0 is the initial strip thickness, n is the strain hardening coefficient.

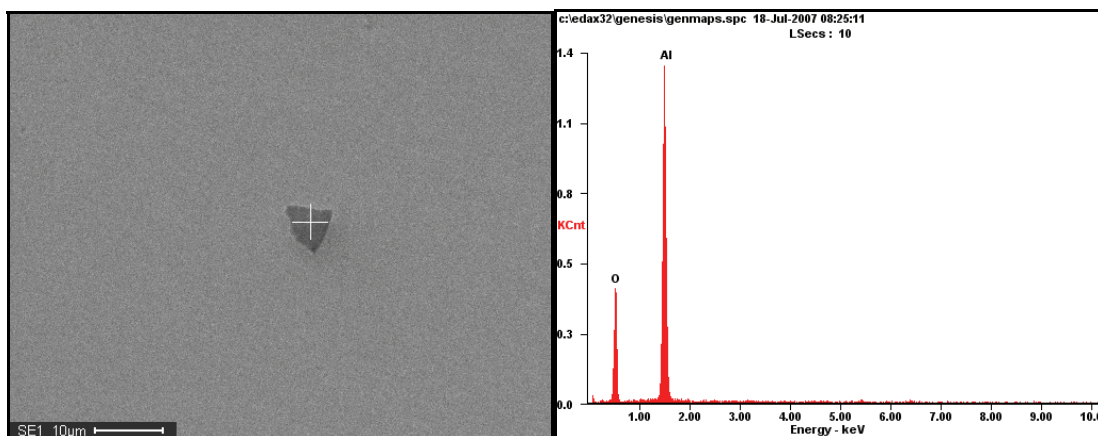


Fig. 51. Inclusion in Type 304 stainless steel strip

Parameters	Roll	Strip	Inclusion
Density, kg/m^3	7850	7830	3800
Young's modulus, GPa	210	193	352
Poisson's ratio	0.3	0.36	0.24
Initial deformation resistance, MPa	-	205	263.9
Strain hardening coefficient in Eq.(1)	-	0.112	-

Table 9. Material parameters in rolling process

4.1.2 FE model

Owing to the symmetry of strip and rolls, a quarter of the strip and the rolls are considered in the geometrical model. The rigid material model is employed for the rolls and the bilinear isotropic material models for the strips and the inclusions. The geometrical models of the strip with an inclusion before rolling are built which are meshed with 8-noded hexahedral elements. There are 6912 elements in the inclusion and 43520 elements in the strip matrix. The FE meshing of strip

with an inclusion before rolling is shown in Fig. 52. In rolling process, the roll rotates with a stable angular velocity, and the strip enters the roll with an initial velocity and exits under the action of friction force. The nodes in the middle cross section of strip thickness are constrained, $U_y=0$; and the nodes in the middle cross section of strip width are constrained, $U_z=0$. The FE models of the second pass and the third are obtained by updating geometrical method.

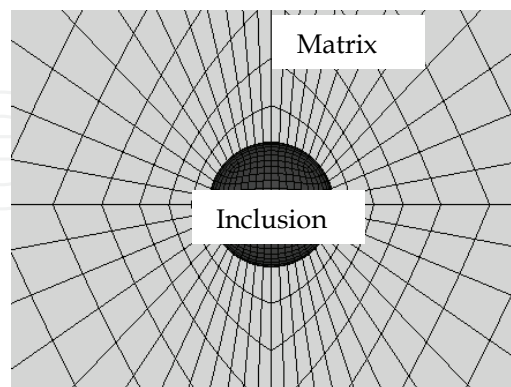


Fig. 52. FE meshing of strip with an inclusion

4.1.3 Results and discussion

(1) Deformation of inclusions during rolling [60]

Table 10 shows the inclusion shape after deformation in the rolling processes. The deformation of inclusion gradually increases from S_1 to S_4 as well as that from Pass 1 to Pass 3. When the inclusion is bond-limited with the strip matrix, after multi-pass cold rolling, the inclusion shape calculated by simulation is in good agreement with the experimental result as shown in Fig. 53. The deformation process of inclusions in detail under various rolling conditions is shown as follows.

Fig. 54 shows the projection of the inclusion shape after every pass in cold rolling process when the inclusion diameter is $20\ \mu\text{m}$. The inclusion spreads along the rolling direction and decreases along the strip thickness direction but slightly changes along the strip width direction. Meanwhile, the unequal deformation of inclusion gradually increases as the rolling pass increases, and the deformation in the front of inclusion is larger than that in the rear of inclusion.

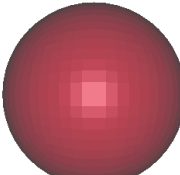
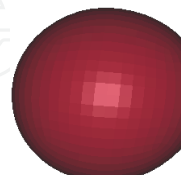
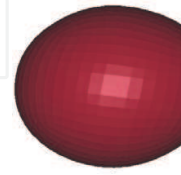
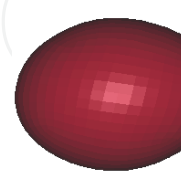
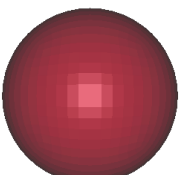
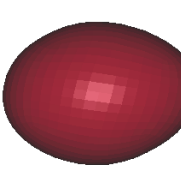
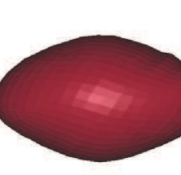
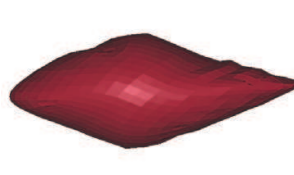
		→ Rolling direction			
		S_1	S_2	S_3	S_4
During pass 1	Inclusion shape				
		Before rolling	Pass 1	Pass 2	Pass 3
During multi-pass	Inclusion shape				

Table 10. Inclusion deformation in rolling process when inclusion size is $20\ \mu\text{m}$

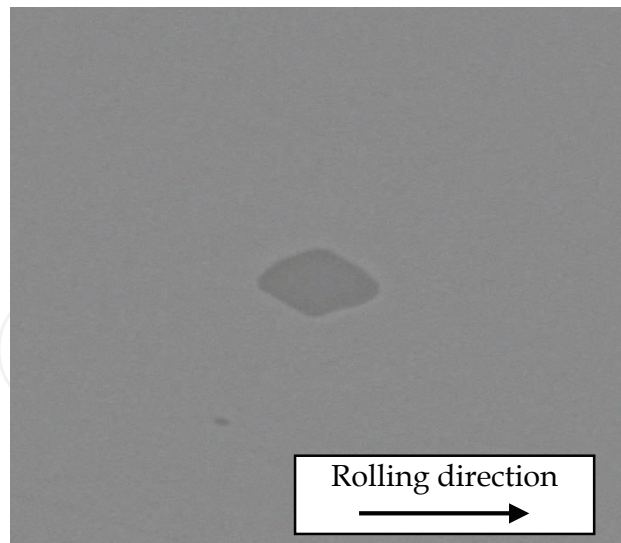


Fig. 53. Inclusion shape after cold rolling

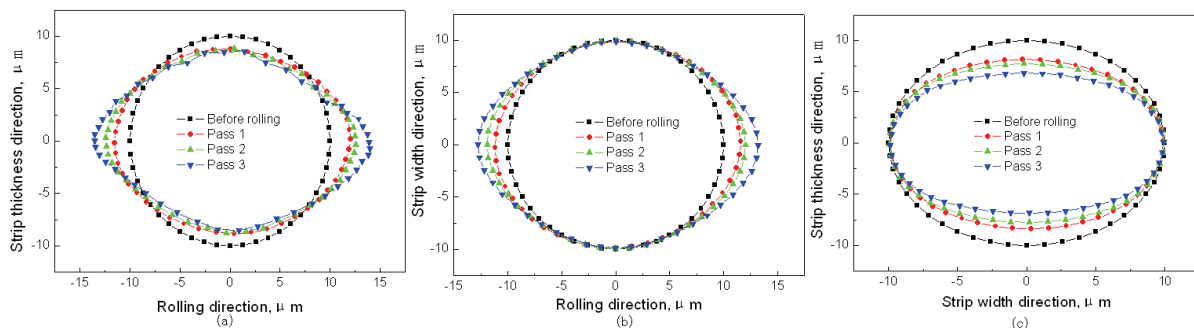


Fig. 54. Inclusion shape in XY (a), XZ (b), and YZ (c) profiles after multi-pass rolling for 20-micron inclusion

In order to better analyze the influence of inclusion sizes on the deformation of inclusions, the scaled profile of inclusions (generating the scaled inclusion profiles with the inclusion diameter) is employed. Fig. 55 shows the inclusion shape in the projection of XY profile for a variety of inclusion sizes in cold rolling process. In the first pass, the inclusions have similar shape when the inclusion diameter is larger than 20 μm , but the deformation of inclusion is much less when the inclusion diameter is less than 10 μm . As for different inclusion size, the difference of inclusion shape gradually increases with increase of rolling pass. And the smaller the inclusion diameter is, the less the inclusion deforms.

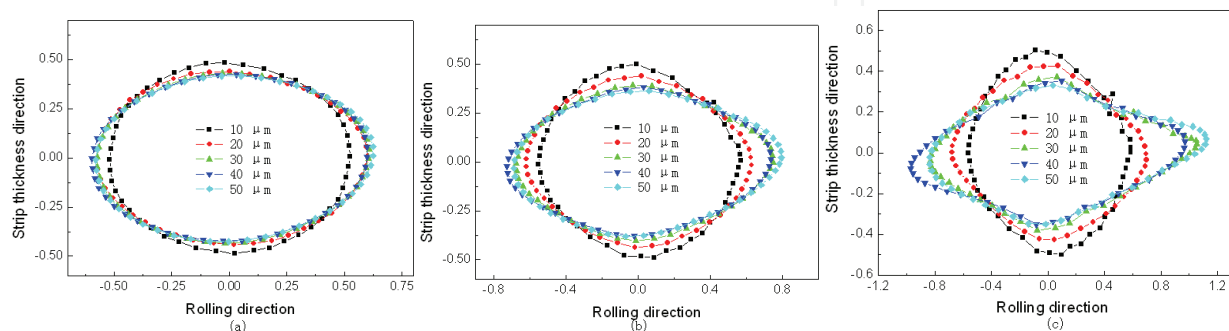


Fig. 55. Inclusion deformation for inclusion sizes after the first (a), second (b), and third (c) pass

Fig. 56 shows the inclusion shape in the projection of XY profile for a variety of the inclusion positions in cold rolling process. The inclusions in different positions of strip have similar deformations in the first pass except the inclusion in position of 1/8 of strip thickness. Meanwhile, the shorter the distance between the inclusion and the strip surface is, the larger the inclusion deforms.

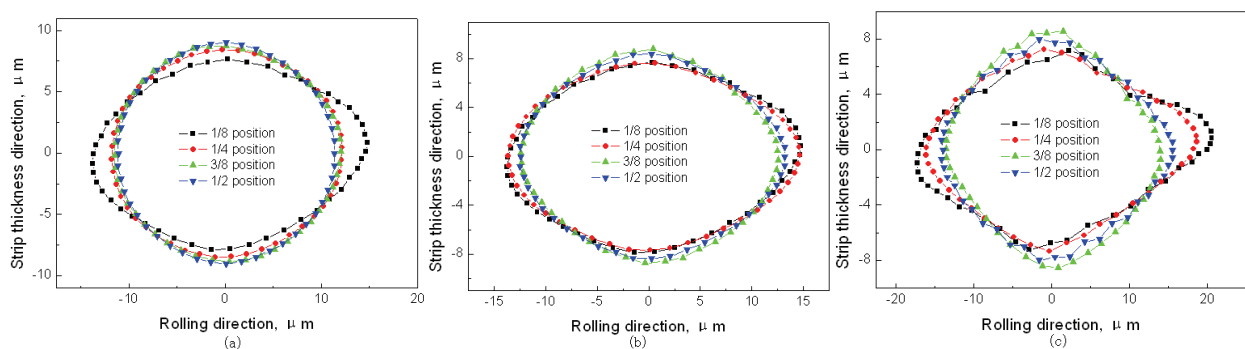


Fig. 56. Inclusion deformation for inclusion positions after the first (a), second (b), and third (c) pass

(2) Movement of inclusion in strip [61]

In rolling process, the influence of the distribution of inclusions on the strip quality is very large. For some kinds of inclusions whose deformation resistances are larger than that of the strip matrix, the deformation of inclusion is less than that of the strip matrix during rolling, which might move to the strip subsurface and then affect the quality of strip surface. Sometimes, the inclusion size is large, the distance between the inclusion and the strip surface will decrease clearly with reduction of the strip thickness; even the inclusion exposes to the strip surface and worsens the strip quality. Meanwhile, the surface cracks of slab might be also caused for the enriched inclusions near the subsurface of strip. In the following, the absolute distance between the inclusion and the strip surface (L_T') and the relative distance between the inclusion and the strip surface (L_T' / H_1) are employed respectively.

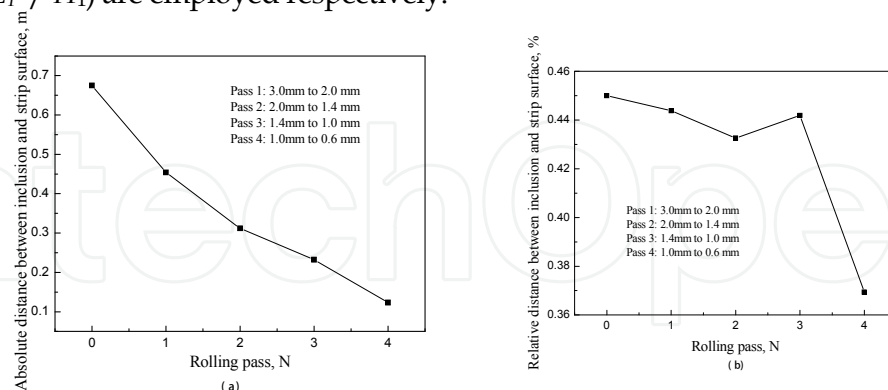


Fig. 57. Movement of inclusion during multi-pass rolling

Fig. 57 shows the change curve of the distance between the inclusion and the strip surface to the strip thickness. In Fig.57 (a), the absolute distance between the inclusion and the strip surface decreases as the rolling pass increases. When the strip thickness is 3.0 mm, the absolute distance between the inclusion and the strip surface is about 0.67 mm; and when the strip thickness is 0.6 mm, the absolute distance is only 0.1 mm. Fig.57 (b) shows the

relative distance between the inclusion and the strip surface. In the figure, the relative distance between the inclusion and the strip surface gradually decreases as the rolling pass increases. Meanwhile, the relative distance clearly decreases when the strip thickness is thin. From the results, it might be one kind of the justifications that the thinner the strip thickness is, the larger the effect of inclusions on the strip surface quality is.

Fig. 58 shows the distance between the inclusion and the strip surface under a variety of inclusion sizes, (a) for the absolute distance, (b) for the relative distance. As shown in the figure, the absolute distance decreases with decrease of the inclusion sizes. When the inclusion diameter is 10 μm , the relative distance changes slightly during multi-pass rolling, but when the inclusion diameter is 100 μm , the relative distance clearly decreases as the rolling pass increases. So, the inclusion will more easily approach the strip surface as the inclusion size increases, and the relative distance scarcely changes when the inclusion size is less than 10 μm .

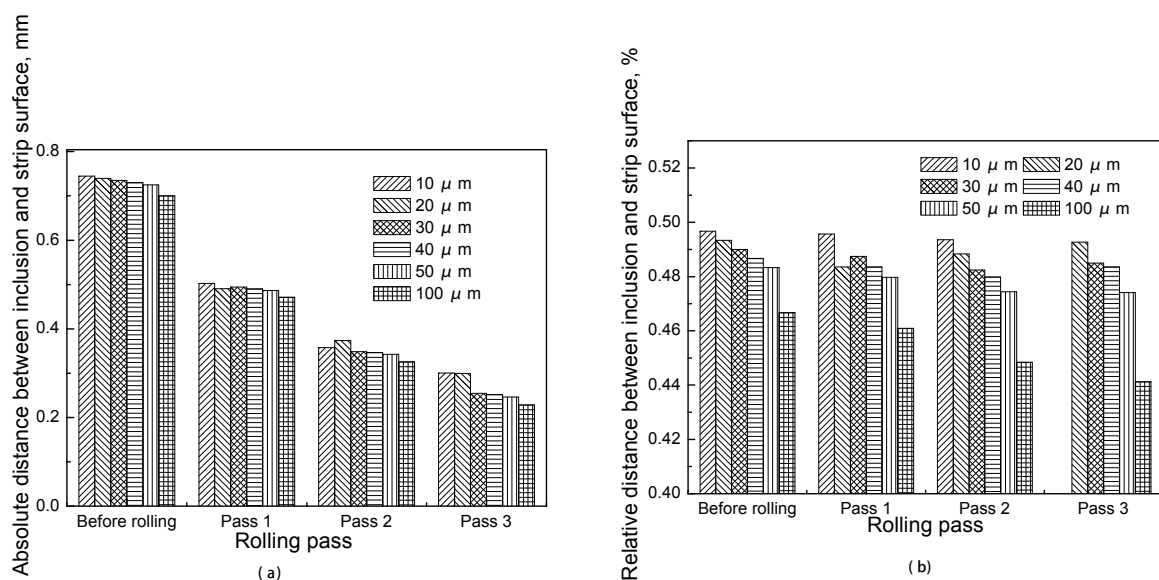


Fig. 58. Movement of inclusion for various inclusion sizes

Fig. 59 shows the distance between the inclusion and the strip surface under various inclusion deformation resistances, where (a) shows the absolute distance and (b) shows the movement distance. The distance between the inclusion and the strip surface for hard inclusions is less than that for soft inclusions when their sizes are the same.

Fig. 60 shows the distance between the inclusion and the strip surface under a variety of inclusion position, where (a) for the absolute distance and (b) for the relative distance, (c) and (d) are the scaled figure of inclusion in the position of 1/8 strip thickness shown in the Figs. (a) and (b). During rolling, the absolute distance decreases with increase of the rolling passes, and the difference between the absolute distances increases with increase of the initial absolute distance. But the inclusion easily approaches to the strip surface when the initial absolute distance decreases. As shown in Fig. (d), the relative distance decreases clearly as the rolling pass increases when the inclusion is in the position of 1/8 of strip thickness.

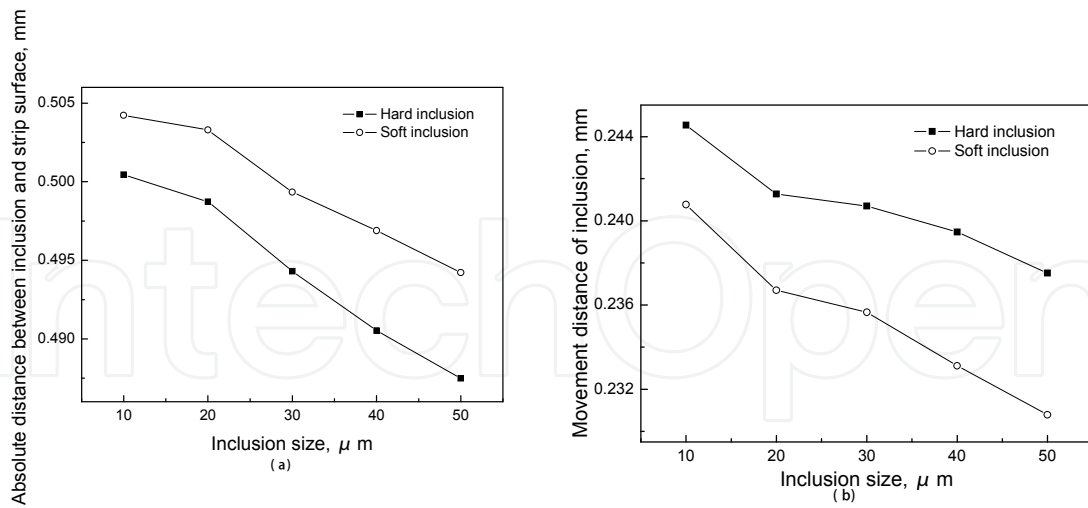


Fig. 59. Movement of inclusion for various deformation resistances of inclusions

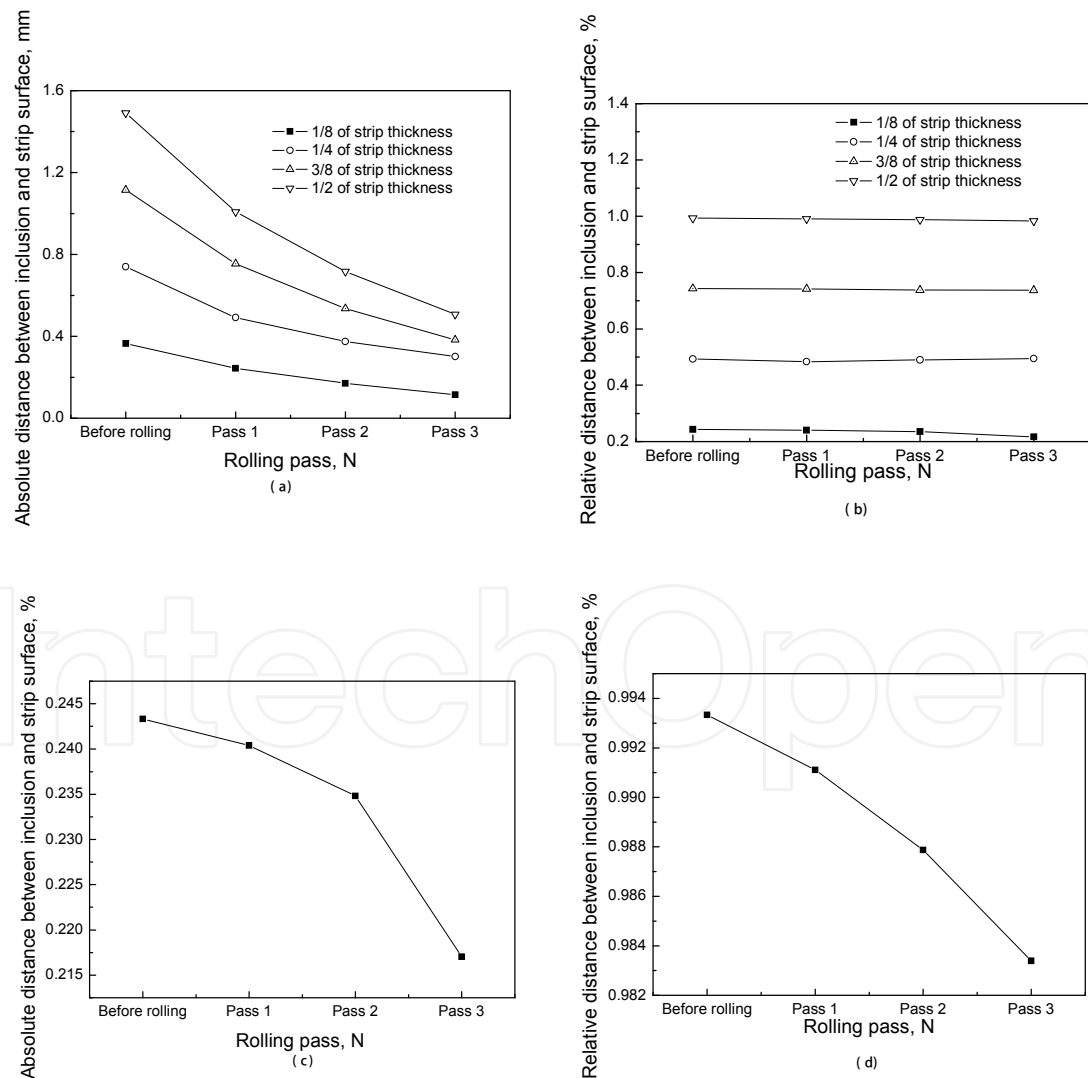


Fig. 60. Movement of inclusion for various inclusion positions (20 μm)

Fig. 61 shows the distance between the inclusion and the strip surface under a variety of work roll diameter, where (a) for the absolute distance and (b) for the relative distance. In the figure, the influence of work roll diameters on the movement of inclusion is small.

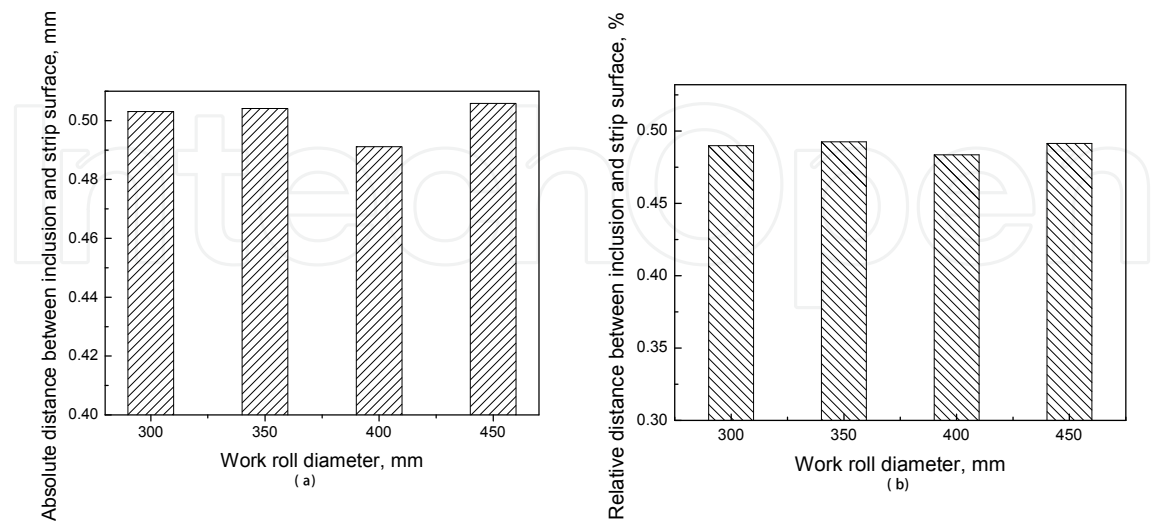


Fig. 61. Movement of inclusion for various work roll diameters (20 μm)

4.1.4 Discussion

During cold rolling, the cracks might appear between the inclusion and the strip matrix when the non-uniform deformation occurs between the inclusion and the strip matrix and whose bonding strength is low, as shown in Fig. 62. When the temperature of strip is high, the cracks might self-heal [62, 63], however, the iron atoms in strip generally do not migrate when the temperature of strip is less than 500 $^{\circ}\text{C}$, so the cracks can not automatically heal during cold rolling. For that it is significant for decrease of the defects in strip to analyze the relationships between the reduction of strip and the deformation of inclusions. [64] proposed the methods to control faults forming in the hot deformation of workpieces, (1) the plastic deformation should be used to control the shape of inclusion and reduce the concentration value of stress and strain caused by inclusion; (2) plastic inclusions should be dispersed to prevent cracks originating from inclusions in exapatiation to meet the quality standard of flaw detection.

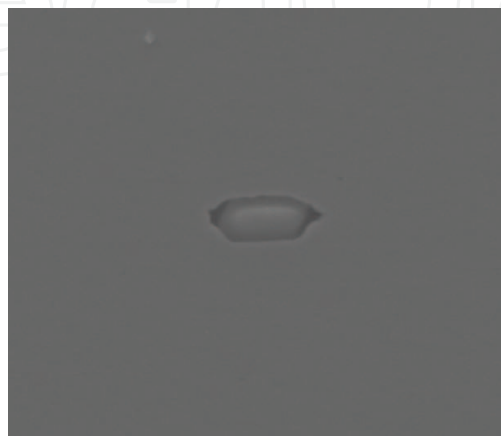


Fig. 62. Cracks near inclusion in strip after rolling

So the influence of the inclusion sizes on the crack generation is obvious, and the harm of inclusions during cold rolling will be more obvious if the large size inclusions are not dispersed into small ones during hot rolling.

From the results above, the deformation of inclusions decreases with reduction of the inclusion size. When the inclusion diameter is less than 10 μm , the deformation of inclusion is very small. By contrary, when the inclusion diameter is larger than 20 μm , the inclusion will deform with the strip matrix and elongate along the rolling direction. Meanwhile, it could be found that the deformation in front of inclusion is larger than that in rear of inclusion. Because the fatigue damage in bulk ductile metals usually originates from the strain localized region, where extrusions/intrusions form and the cracks might appear [65], the crack (void) size in front of inclusion is larger than that in rear of inclusion [56]. From the analysis above, the strip with a certain-size inclusion could but bear a certain reduction ratio; otherwise the cracks will appear in the strip. Meanwhile, from the results above, the closer the inclusion approaches the strip surface, the greater the deformation of inclusion occurs [66]. Besides the inclusion size and the inclusion position, some other influencing factors might affect the inclusion deformation, such as: the rolling reduction ratio and the rolling speed. Ervasti finds the void size increase with an increase of the rolling reduction ratio and decrease of the rolling speed.

The equivalent strain distribution of the strip matrix and the inclusion in the deformation zone is shown in Fig. 63. In the figure, the strain value of inclusion is much less than that of strip matrix, which is about 0.07 in the center of inclusion that is about 1/10 of the strain value of the strip matrix. Meanwhile, a zone of large strain value exists in the front and the rear of inclusion, for some kinds of strip matrix, where the cracks are easy to appear. Table 11 shows the maximum and the minimum strain and the strain gradient between the inclusions and the strip matrix for a variety of the inclusion sizes. When the inclusion diameter is 50 μm , the difference of strain between the inclusion and the strip matrix reaches 1.025. So, the strip quality will deteriorate with increases of the inclusion sizes.

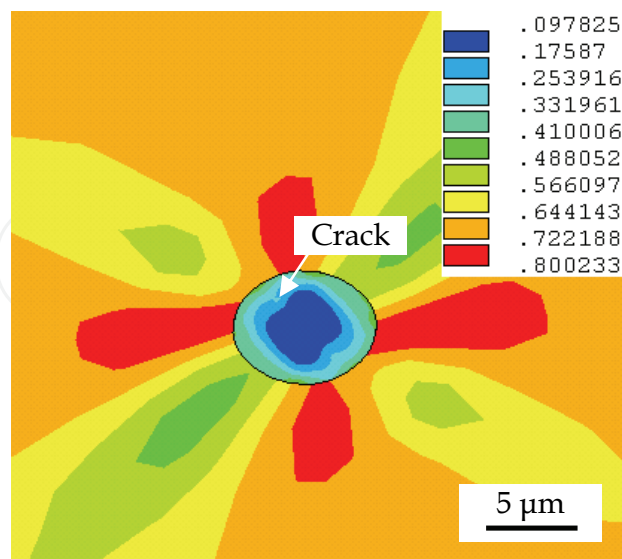


Fig. 63. Contour of the strain distribution of strip with a 20-micron inclusion after first pass in XY profile [67]

Inclusion size, μm	10	20	30	40	50
Strip matrix	0.803	0.800	0.945	1.026	1.246
Inclusion	0.044	0.098	0.168	0.243	0.221
Strain difference	0.759	0.702	0.777	0.783	1.025

Table 11. Strain gradient between the inclusion and the strip matrix for a variety of inclusion sizes [67]

4.2 Evolution of inclusions separate with matrix during rolling [68]

During continuous casting, the inclusions might exist in stainless steel. The behavior of inclusions will strongly affect the strip quality during rolling, especially the macroscopic inclusions. During rolling, the inclusions might be disjoined with the strip matrix, and then cracks generate; sometimes, the inclusions might move to the strip surface, which cause the scratch marks.

This part presents a new method to simulate the behavior of inclusions and the crack generation during rolling. The bond strength between the inclusions and the matrix can be adjusted through changing the material attribution of the transition layer which is established between the inclusions and the matrix. Meanwhile, the material failure is taken into account in the elements of the transition layer during deformation, with which the crack generation can be analyzed. The behavior of inclusions in type 304 stainless steel strips has been simulated by 3D FEM, and the influence of the bond strength between the inclusions and the matrix on the crack generation is analyzed.

4.2.1) Experimental

The SEM photograph of the inclusion in type 304 stainless steel strip was taken, as shown in Fig. 64. After corrosion, there is clear space between the inclusion and the strip matrix which is corroded. So there might be a transition layer between the inclusion and the matrix. According to the phenomenon, it can be assumed that there exists a transition layer between the inclusion and the strip matrix when simulating the deformation of inclusion during rolling, and that the bond strength between the inclusion and the matrix can be changed through adjustment of the material attribution of the transition layer.

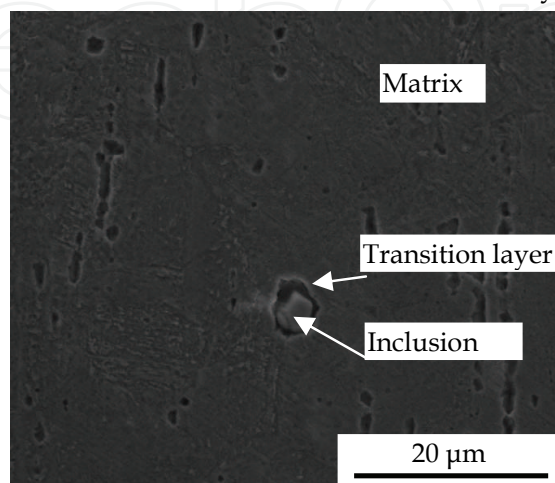


Fig. 64. SEM photograph of inclusion in 304 stainless steel strip with corrosion

4.2.2 FE analysis

(1) Basic parameters

In the simulation, the work roll diameter is 400 mm which is assumed to be rigid. The strip thickness is 3 mm before rolling and 2 mm after rolling. The diameter of inclusion is 48 μm which is assumed to be spherical and in the position of 1/4 of strip thickness (The inclusion size changes from a few to tens of microns, and a large value is employed for saving computer time.). And the thickness of the transition layer is 2 μm . During rolling, the inclusion is Al_2O_3 ; and the metrical parameters of transition layer are assumed to be the steel and the inclusion, each of which is occupying half and the material failure is considered. The friction coefficient is 0.15 between the strip and the roll. The main material parameters are shown in **Table 12**.

Parameters	Roll	Strip	Inclusion	Transition
Density, kg/m^3	7850	7830	3800	5815
Young's modulus, GPa	210	193	352	272.5
Poisson's ratio	0.3	0.36	0.24	0.3
Deformation resistance, MPa	-	205	263.9	238.8
Failure strain (F_s)	-	-	-	various

Table 12. Main material parameters in rolling process

(2) FE model

Owing to the symmetry of strip and rolls, a quarter of the strip and the rolls are considered in the geometrical model. The rolling model of the strip with inclusion is built with the parameters above. The model is meshed with 8-noded hexahedral elements. It just refines the elements in the inclusion, the transition layer and the matrix near the inclusion. And there are 6912 elements in the inclusion, 1728 elements in the transition layer and 80640 elements in the strip matrix. In rolling process, the roll rotates with a stable angular velocity, and the strip enters the roll with an initial velocity and exits under the friction force. The nodes on the middle cross section of strip thickness are constrained, $U_Y=0$; and the nodes in the middle cross section of strip width are constrained, $U_Z=0$ (X is rolling direction, Y is the strip thickness direction, Z is the strip width direction). The geometry and meshing of strip with the inclusion and the transition layer before rolling is shown in **Fig. 65**.

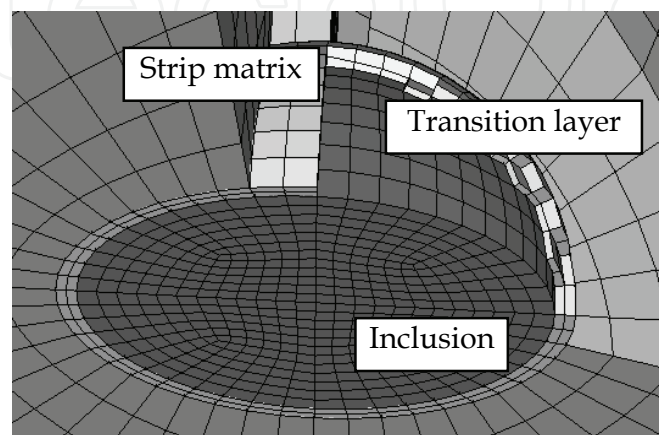


Fig. 65. FE meshing of strip with inclusion

4.2.3 Results

When the deformation of transition layer reaches the failure condition, a crack will appear between the inclusion and the strip matrix. The crack sizes can be obtained under the different failure conditions of transition layer. Fig. 66 shows the transition layer shape after single-pass cold rolling process when the failure strain equals 0.15 (a), 0.1(b), 0.05(c) and 0.025(d). In the figure, the crack size in the transition layer between the inclusion and the matrix increases with the decrease of the bond strength between the inclusion and the strip matrix. When the failure strain is larger than 0.15, the cracks do not appear on the transition layer which deforms with the strip. When the failure strain is less than 0.1, the cracks appear on the transition layer, and the crack direction is about 45 degree with the rolling direction which is affected by the position of inclusion and the shape of deformation zone in the rolls gap. And with the decrease of the failure strain of transition layer, the cracks propagate. When the failure strain is less than 0.025, the inclusion almost sloughs off the strip matrix.

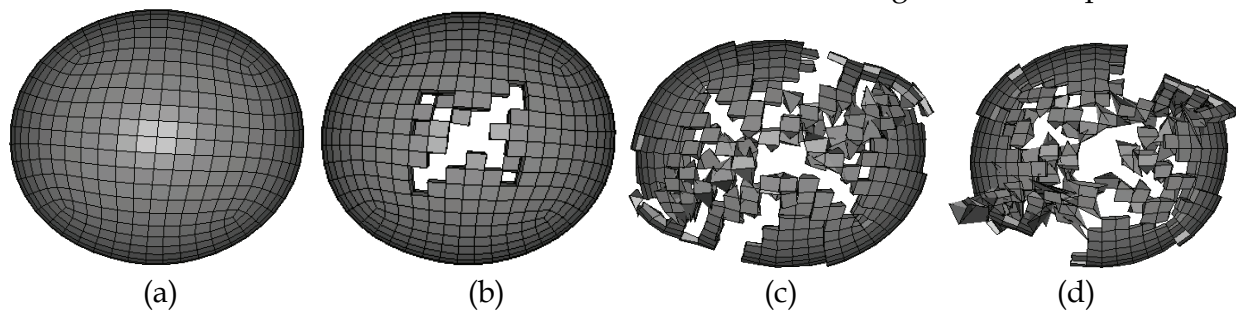


Fig. 66. Failure conditions of transition layer after rolling

Fig. 67 shows the inclusion shape after rolling. In the figure, the inclusion elongates along the rolling direction which is changed from a sphere to an ellipsoid; and the inclusion spreads slightly along the strip width direction compared with that along rolling direction.

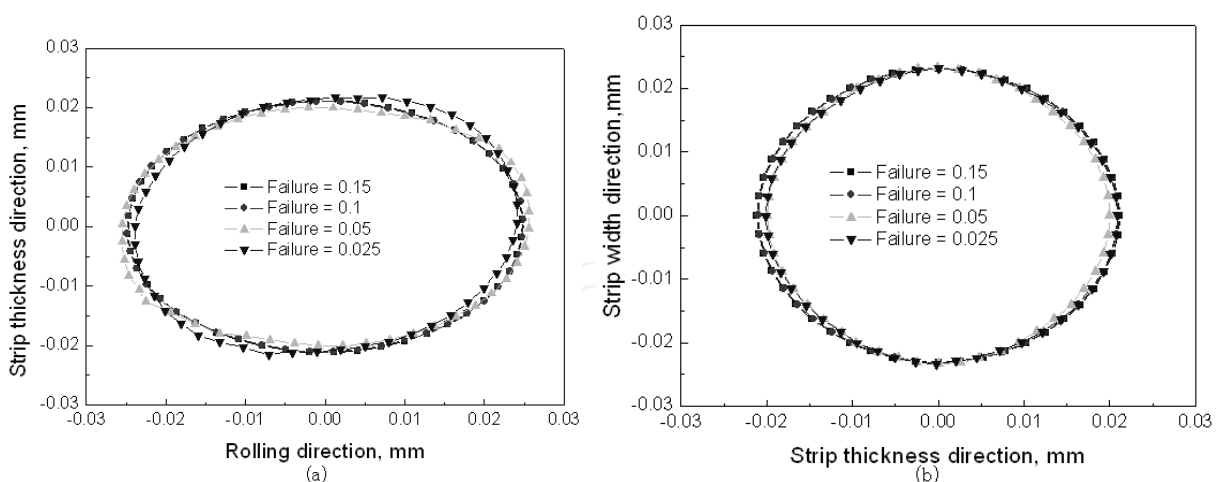


Fig. 67. Inclusion shape after rolling along rolling direction (a) and along strip width direction (b)

4.3 Evolution of inclusion with weak adhesion to strip matrix

4.3.1 Basic parameters and rolling conditions

Fig. 68 shows the schematic drawing of strip rolling with a circle (square, triangle) inclusion, where X is the rolling direction, Y is the strip thickness direction. Fig. 69 shows three typical

kinds of shapes of inclusions in the type 304 stainless steel determined by SEM.

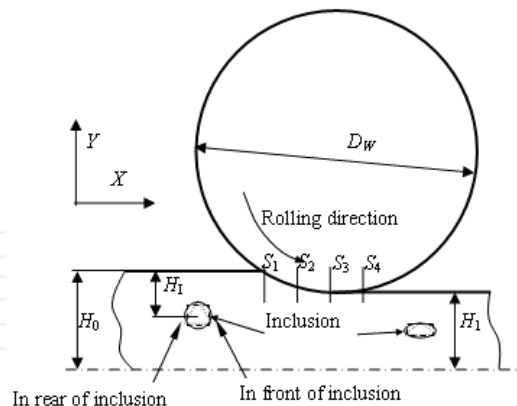


Fig. 68. Schematic drawing of strip rolling with an inclusion

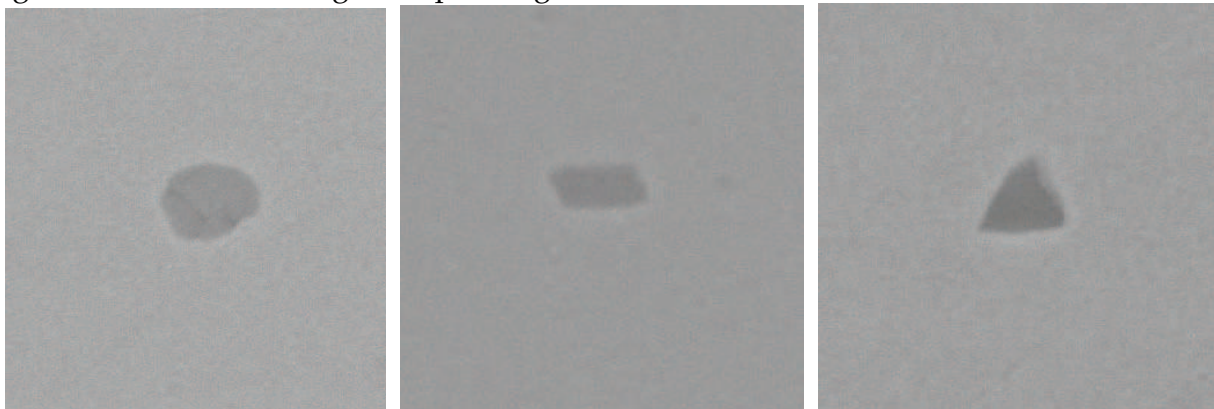


Fig. 69. Shape of inclusions in a stainless steel

In the simulation, the work roll diameter (D_W) is 400 mm. The strip thickness is 3.0 mm before rolling and 2.0 mm after rolling. The circle, square, and triangle inclusions [57, 69] are employed respectively whose sizes are 10, 20, 30 and 40 μm separately and in the position of 1/2, 3/8, 1/4 and 1/8 of strip thickness (H_1/H_0). The Coulomb friction model is used in the FE models and the friction coefficient between the strip and the roll is assumed to be 0.15. The friction coefficient during cold rolling is about 0.04 ~ 0.231[70].

During rolling, the strip matrix is the type 304 stainless steel. And the hard and soft inclusions are employed respectively. The main material parameters of the roll, the strip matrix and the inclusions used in FE models are shown in **Table 13**.

Parameter	Roll	Strip matrix	Inclusion	
			Hard	Soft
Density, kg/m^3	7850	7830	3800	5000
Young's Modulus, GPa	210	193	352	120
Poisson's ratio	0.3	0.36	0.24	0.36
Deformation resistance, MPa	-	205	263.9	100

Table 13. Material parameters of roll, strip matrix and inclusion

4.3.2 FE model

Due to symmetry of strip and rolls, a half of the strip and the rolls are considered in the model. The rigid material model is employed for the roll and the bilinear isotropic material model for the strip matrix and the inclusions. The 2D geometrical models of the strip with an inclusion before rolling are built with the parameters above and are meshed with quadrilateral elements. The inclusions and the strip matrix are assumed to be weak adhesion [56], and the constant friction coefficient exists at the interface between inclusions and strip matrix. The FE meshing of strips with circle, square, and triangle inclusions before rolling and the whole rolling model are shown in Fig. 70. The element sizes around inclusions are much finer than the others for saving the computing time. In rolling process, the roll rotates with a constant angular velocity and the strip enters the roll with an initial velocity and exits under the action of friction force between the roll and strip. During rolling, cracks form for the contact between matrix surfaces and do not propagate.

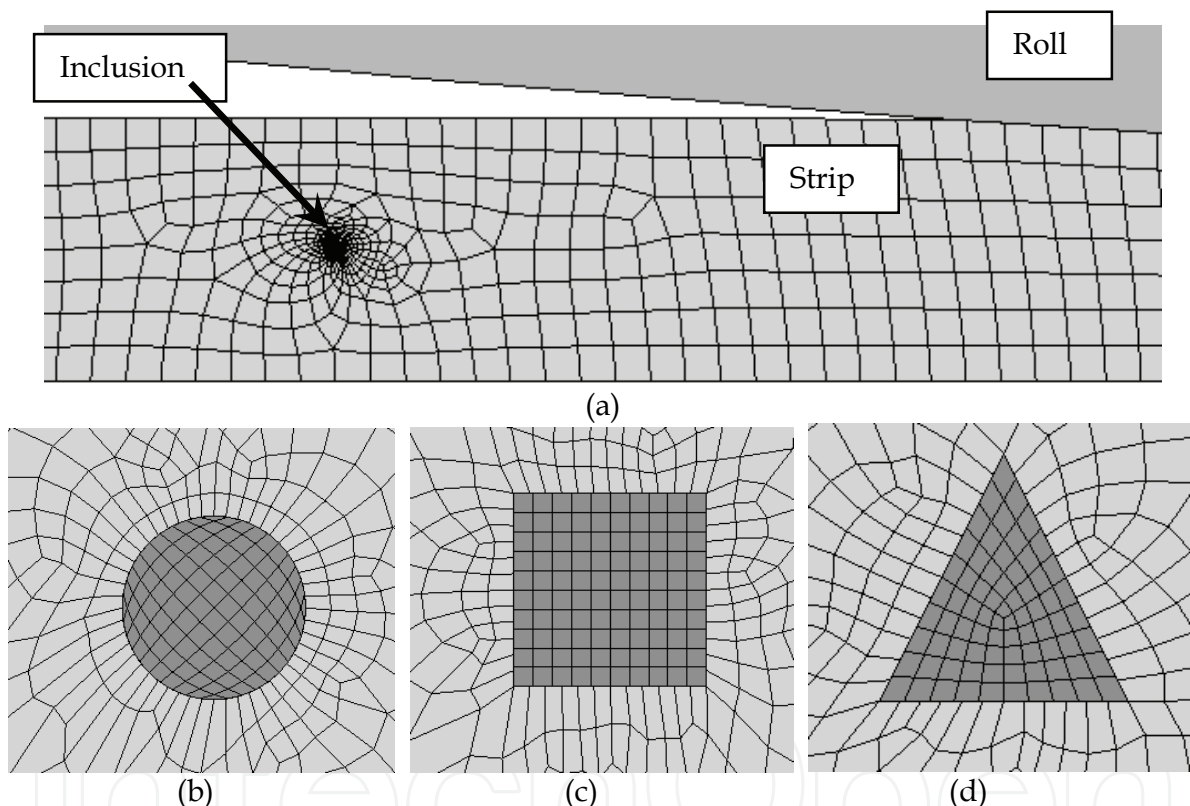


Fig. 70. FE meshing of the whole rolling model (a), and slab with circle (b), square (c), triangle (d) inclusions

4.3.3 Results and Discussion [71]

Fig. 71 shows the relationship between the hard circle inclusion and strip matrix at different positions in the deformation zone during rolling. In the position S_2 , there are two voids in front and rear of the inclusion, and the tip of voids gradually close, which change into cracks after rolling, as shown in Fig.71 (d). In the following, the relationship between the inclusion and the strip matrix in the position of S_4 during rolling is employed.

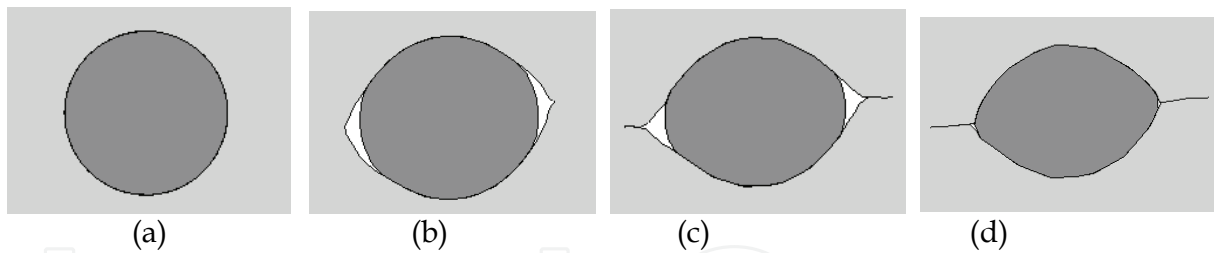


Fig. 71. Relationship between the inclusion and the strip matrix in S1(a), S2(b), S3(c), S4(d) position during rolling

Fig. 72 shows the relationship between the hard inclusion and the strip matrix after rolling when the inclusion size is $10\ \mu\text{m}$. If the inclusion shape is circle, there are two cracks in front and rear of the inclusion respectively. If the inclusion shape is triangle, there is one crack in rear of the inclusion. **Fig.73** shows the inclusion shape in type 304 stainless steel after cold rolling through SEM. Compared the relationship between the inclusion and the strip matrix in the **Fig. 72** and that in the **Fig. 73**, the calculated results are in good agreement with the one in the experiment.

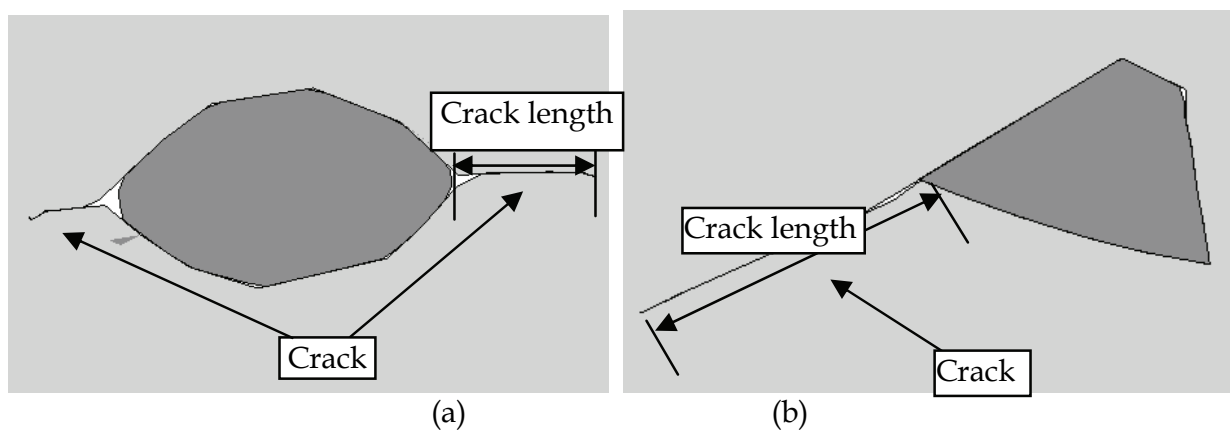


Fig. 72. Relationship between the inclusion and the strip matrix after rolling for 10-micron circle (a) and triangle (b) hard inclusions in the position of $1/4$ of strip thickness

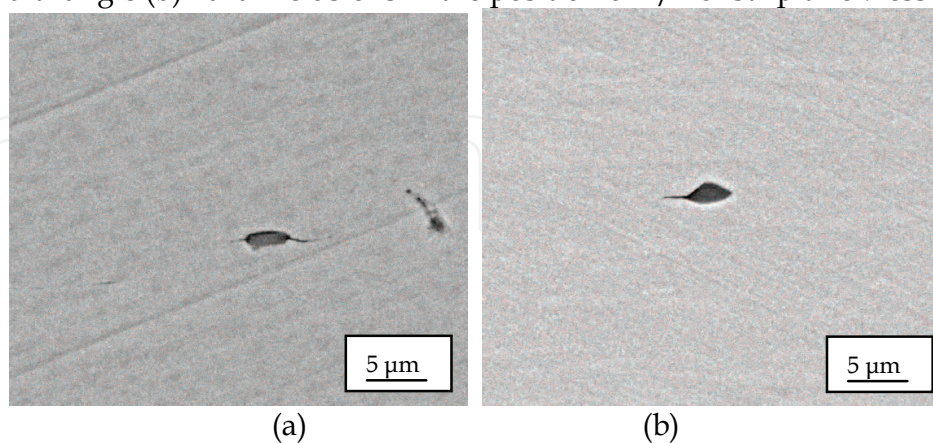


Fig. 73. SEM graph of cracks around circle (a) and triangle (b) hard inclusions in strip matrix after rolling

Fig. 74 shows the relationship between the soft inclusion and the strip matrix after rolling process when the inclusion size is $10\ \mu\text{m}$. If the inclusions are soft, there are no cracks

around the inclusions. Because the inclusion shapes are obtained in single pass, it is obvious that the inclusions will spread into a narrow strip after multi-pass rolling process, which will be similar to that of the experimental results through SEM as shown in Fig. 75.

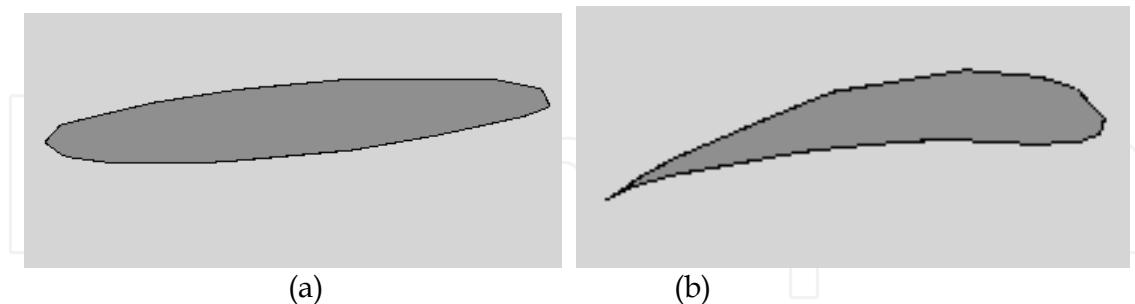


Fig. 74. Relationship between the inclusion and the strip matrix after rolling for 10-micron circle (a) and triangle (b) soft inclusions in the position of $1/4$ of strip thickness

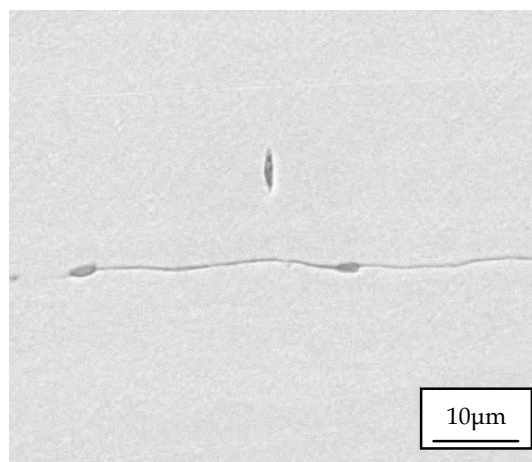


Fig. 75. SEM graph of the shape of soft inclusion in strip matrix after rolling

Table 14 shows the relationship between the inclusions and the strip matrix for various inclusion sizes both hard and soft inclusions when the inclusions are positioned at $1/4$ of the strip thickness. For hard inclusions, when the inclusions are circle, the cracks appear in front and rear of the inclusions and the crack direction is along the rolling direction. If the inclusions are square, two cracks appear in front and rear of inclusions separately and the crack direction is 45 degree to the rolling direction at the rolling conditions, meanwhile, the square inclusions deform to the ellipse inclusions similar to that of circle inclusions; when the inclusions are triangle, there just is one crack appear in rear of inclusions in the position of the strip thickness. When the inclusions are soft, there are no cracks around inclusions under various inclusion sizes for all the circle, square and triangle inclusions.

Table 15 shows the relationship between the inclusions of $20 \mu\text{m}$ and the strip matrix under various inclusion positions for both hard and soft inclusions. For hard inclusions, when the inclusions are circle, the cracks appears in front and rear of the inclusions, and the crack size decreases with increase of the distance between the inclusions and the strip surface; when the shape of inclusions is square, two cracks appear in front and rear of inclusions which are in the position of $3/8$, $1/4$ and $1/8$ of the strip thickness, and four cracks appear in every corner of the square inclusions when the inclusions are in the position of $1/2$ of the strip

thickness; when the inclusions are triangle, one crack appears in rear of the inclusions that are in the position of $1/4$ and $1/8$ of the strip thickness and two cracks appears in front and rear of the inclusions that are in the position of $1/2$ and $3/8$ of the strip thickness. As to the soft inclusions, there are no cracks around inclusions after rolling process under various the positions of the inclusions along the strip thickness direction.

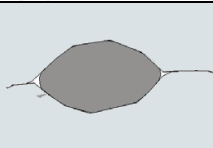
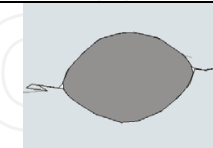
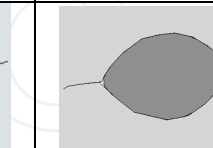
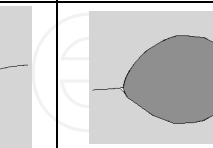
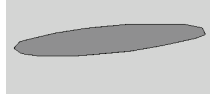
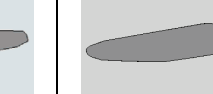
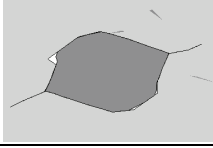
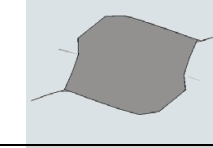
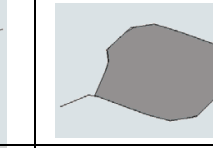
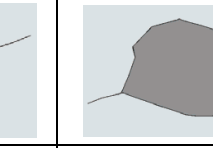
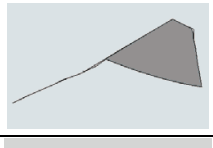
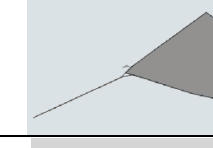
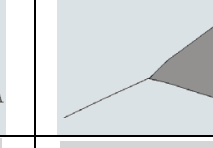
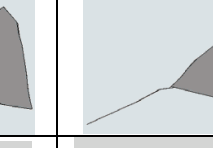
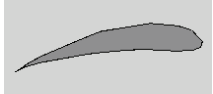
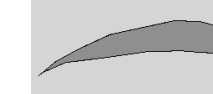
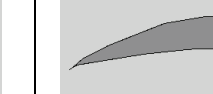
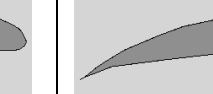
Inclusion size, μm		10	20	30	40
Circle inclusions	Hard				
	Soft				
Square inclusions	Hard				
	Soft				
Triangle inclusions	Hard				
	Soft				

Table 14. Relationship between the inclusion and the matrix after rolling for various inclusion sizes when inclusions are in the position of $1/4$ of the strip thickness

In tables 14 and 15, it also can be found that the inclusions rotate a little angle for both hard and soft inclusions. In table 14, the inclusions seemingly rotate with the same angle after rolling, so the inclusion sizes affect the rotation of inclusion slightly. And in table 15, when the inclusion is at the position of $1/2$ of strip thickness, the inclusions do not rotate after rolling process, and with the inclusions approaching to the strip surface, the rotation angle of inclusions increases. So the rotation of inclusion is clearly affected by the position of inclusion in strip.

Fig. 76 shows the crack length around the circle inclusions after rolling for various inclusion sizes and positions. **Fig. 76 (a)** shows the crack length in front of the inclusion, the crack length is about $3 \mu\text{m}$ when the size of inclusion is $10 \mu\text{m}$ which is in the position of $1/8$ of the strip thickness, and the crack length is about $17 \mu\text{m}$ when the inclusion size is $40 \mu\text{m}$ and the inclusion is in the position of $1/2$ of the strip thickness. The crack length increases as the inclusion size increases when the inclusions are in the same position of the strip, and which also increases with increase of the distance between the inclusion and the strip surface. **Fig. 76 (b)** shows the crack length in rear of the inclusions. The crack length in rear of inclusion

increases with increase of the inclusion sizes and the distance between the inclusion and the strip surface similar to that in front of inclusion.

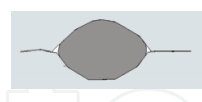
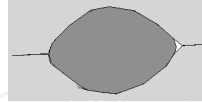
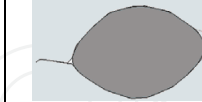
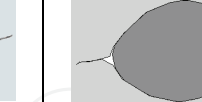
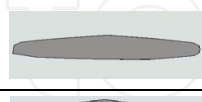
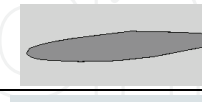
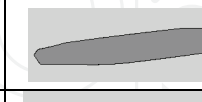
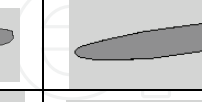
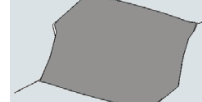
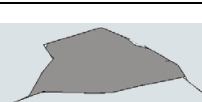
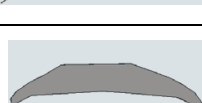
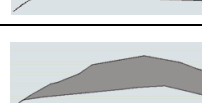
Inclusion position, $H_i/2H_0$		1/2	3/8	1/4	1/8
Circle inclusions	Hard				
	Soft				
Square inclusions	Hard				
	Soft				
Triangle inclusions	Hard				
	Soft				

Table 15. Relationship between inclusion and matrix after rolling for various inclusion positions in strip when inclusion size is $20\ \mu\text{m}$

Fig. 77 shows the crack length in front and rear of the square inclusions after rolling under various inclusion sizes and positions. As shown in the figure, the crack length in front of inclusion increase with increase of the inclusion sizes and the distances between the inclusion and the strip center. Compared **Fig. 77 (a) and (b)**, the crack length are similar between that in front of inclusion and that in rear of inclusion.

Fig. 78 shows the crack length in front and rear of the triangle inclusions after rolling under various inclusion sizes and positions. There are no cracks in front of inclusions when the inclusions are in the position of $1/8$ and $1/4$ of the strip thickness, and the crack length increases with increase of the inclusion sizes when the inclusions are in the position of $3/8$ and $1/2$ of the strip thickness. The crack length in rear of inclusions increases with increase of the inclusion sizes and with decrease of the distance between the inclusion and the strip surface. Compared the **Fig. 78 (a) and (b)**, the crack length in rear of the inclusions is larger than that in front of the inclusions when the inclusions are not in the position of $1/2$ of strip thickness.

As shown in Figs 76 ~ 78, the crack size around inclusion after rolling process decreases with decreasing the inclusion size. If the inclusion size further decreases, the crack size also will decrease, and there will no cracks if the inclusion size is less than a certain value. Meanwhile, it is obvious that there are no cracks around soft inclusions after rolling, but cracks appear for hard inclusions. So with increasing the hardness of inclusion, the cracks will gradually increase which will reach the maximum value when the inclusions are rigid.

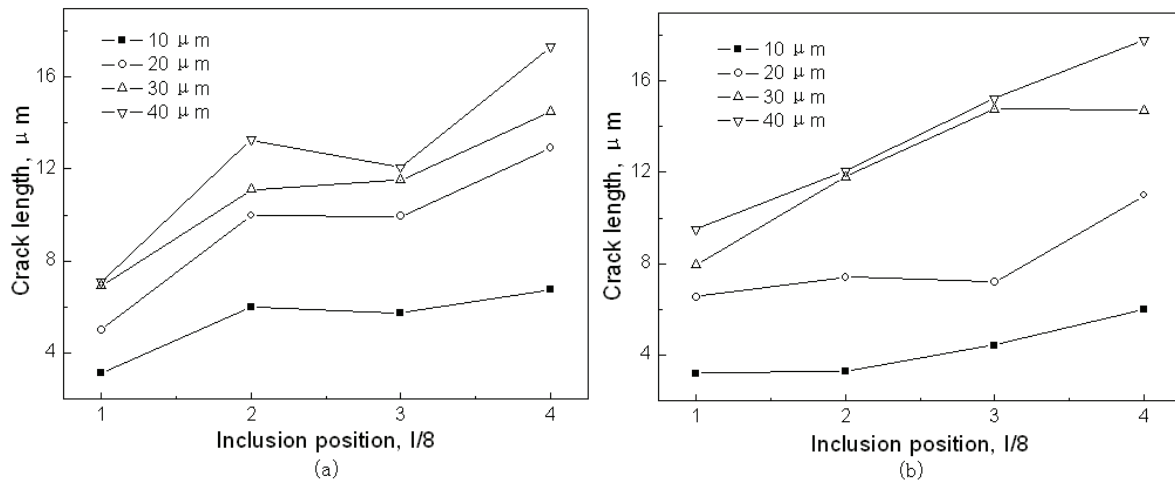


Fig. 76. Crack size in front (a) and rear (b) of circle inclusions

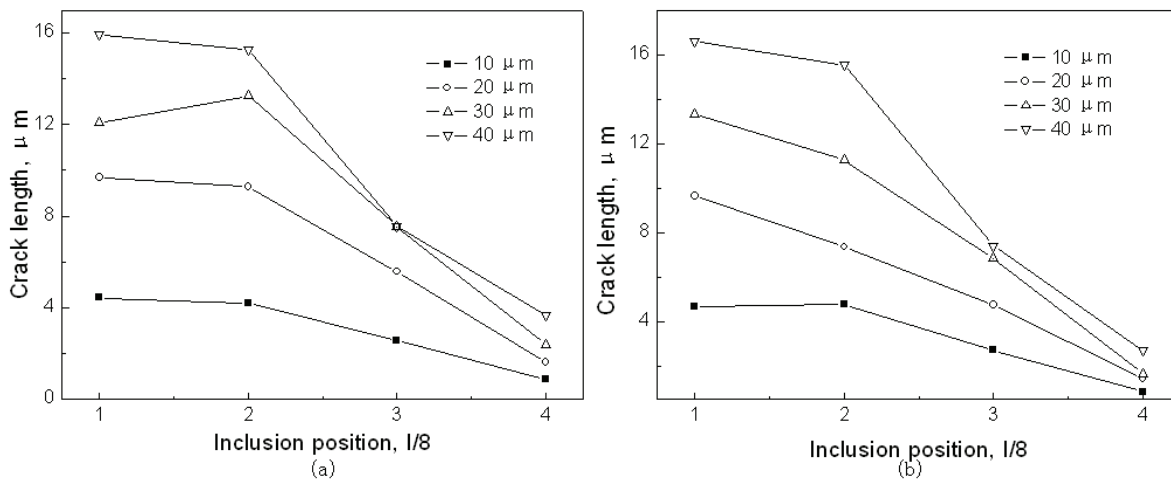


Fig. 77. Crack size in front (a) and rear (b) of square inclusions

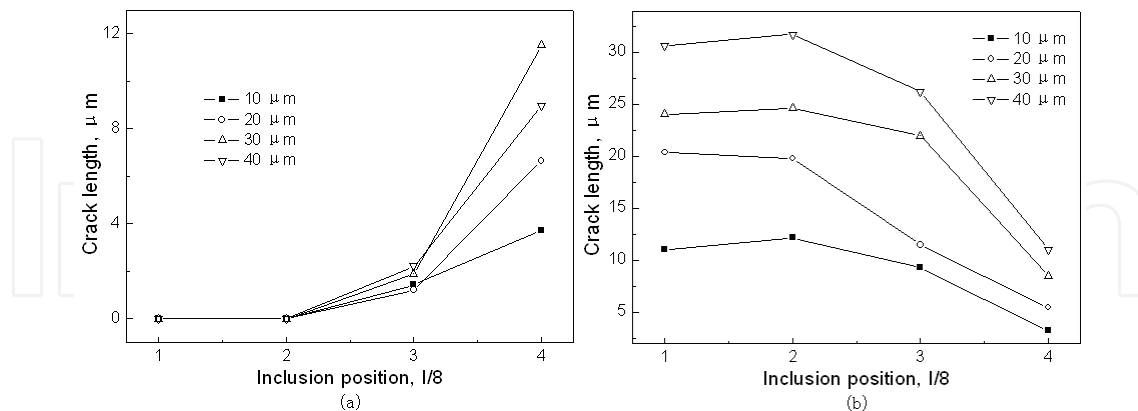


Fig. 78. Crack size in front (a) and rear (b) of triangle inclusions

Acknowledgements

The author gratefully acknowledges the financial supports by the Research Fund for the Doctoral Program of Higher Education through Grant No. 20090042120005. And the author also needs to thank the Prof. LIU Xianghua for his encouragement and guiding and helps, who is the previous director of State Key Laboratory of Rolling and Automation. His current

research fields include modelling and simulation of metal forming processes, advanced structural materials development and AI application in steel rolling process. He has been awarded three National Prizes of Science and Technology of China since 2000.

5. References

- [1] Yu H.L., Liu X.H. Coupling analysis to multipass V-H rolling process by FEM. *Hot Working Technology* 2007, 36(1):85-88. (in Chinese)
- [2] Li C.S., Yu H.L., Deng G.Y., Liu X.H. Numerical simulation to temperature field and thermal stress field of work roll in hot strip rolling. *Journal of Iron and Steel Research International*, 2007, 14(5): 18-23.
- [3] Yu H.L., Liu X.H. Friction and slab deformation during rough rolling. *International Journal of Surface Science and Engineering*, 2009, 3(5/6): 423-434.
- [4] Grass H., Kremaszky C., Reip T., Werner E. 3-D Simulation of hot forming and microstructure evolution. *Computational Materials Science* 2003, 28:469-477.
- [5] Yu H.L., Zhao X.M., Liu X.H. Tri-dimensional elastic-plastic FEM of rolling force during strip finishing rolling process. *Research on Iron and Steel*, 2005, 33(1): 14-16. (in Chinese)
- [6] Yu H.L., Liu X.H., Zhao X.M. Numerical analysis to rolling pressure distribution of plane view pattern controlling pass of plate rolling. *Journal of Plasticity Engineering*, 2005, 12(4): 51-53, 75. (in Chinese)
- [7] Yu H.L., Liu X.H., Li C.S. Influence of groove fillet radii of edger roll on slab deformation. *Iron and Steel*, 2006, 6: 47-51. (in Chinese)
- [8] Yu H.L., Liu X.H., Jiao Z.J., Zhao X.M. Application of geometry model updating method in FEM analysis of plane pattern of plate. *Journal of Iron and Steel Research*, 2006, 18(2): 26-29. (in Chinese)
- [9] Yu H.L., Liu X.H., Lee G.T. Analysis to rolls deflection of Sendzimir mill by 3D FEM. *Transactions of Nonferrous Metals Society of China*, 2007, 17(3): 600-605.
- [10] Knapiński M. The numerical analysis of roll deflection during plate rolling, *Journal of Material Processing Technology*, 2006, 175: 257-265.
- [11] Yu H.L., Liu X.H., Yu Q.B. Tracing of macrosegregation in slab during multipass rolling. Submitted.
- [12] Li C.S., Song S.N., Mei R.B., Zhang G.L., Liu X.H. Online Arithmetic by fast finite element in strip rolling. *Journal of Mechanical Engineering*, 2009, 45(6): 193-198.
- [13] Liu X.H. 2.7 dimensional RPFEM analysis and its application in rolling. *Journal of Northeastern University of Technology*, 1990, 11(5): 468-473.
- [14] Wang L. Application of modified Cholesky factorization forcing matrix to be positive definite in rolling. Shenyang: Northeastern University, 2008.
- [15] Si LY, Lu C, Huynh NN, et al. Simulation of rolling behaviour of cubic oriented al single crystal with crystal plasticity FEM. *Journal of Materials Processing Technology*, , 2008, 201(1-3): 79-84.
- [16] Lue C, Si LY, Zhu HT, et al. Theoretical analysis of texture evolution in cold rolling process of single crystal aluminum. *Transactions of Nonferrous Metals Society of China*, 2007, 17, Sp.1: S254-S257.

- [17] Yu H.L., Liu X.H., Wang G.D. Analysis of crack tip stress of transversal crack on slab corner during V-H rolling process by FEM. *Journal of Iron and Steel Research International*, 2008, 15(3): 19-26.
- [18] Yu H.L., Liu X.H., Chen L.Q., Li C.S., Zhi Y., Li X.W. Influence of edge rolling reduction on plate-edge stress during finish rolling process, *Journal of Iron and Steel Research International*, 2009, 16(1), 22-26.
- [19] Yu H.L., Liu X.H. Behavior of subsurface blisters in slab during hot rolling using FEM. *The Second International Conference on Modelling and Simulation*, Manchester, 2009 May, 37-42.
- [20] Yu H.L., Liu X.H., Li C.S., Chen L.Q. Research on behavior of slab surface defects in forward slip zone during V-H rolling process. *Materials Science Forum*, 2008, 575-578: 243-248.
- [21] Yu H.L., Liu X.H., Bi H.Y., Chen L.Q. Research on behavior of inclusion in stainless steel during rolling by FEM. *Steel Research International*, 2008, 79, Special edition, Vol.1: 389-396.
- [22] Qunpanich D., Mutoh Y., Yoshii K. Fatigue behavior of hot-rolled steel plate at various stages of fabrication. *Materials Science and Engineering A* 2008, 477(1-2): 9-14.
- [23] Yamamoto K. Study on surface defects of coated sheets caused by the surface condition of a hot roughing mill roll. *SEAFISI Quarterly (South East Asia Iron and Steel Institute)* 2007, 36 (3):54-58.
- [24] Riedel H., Andrieux F., Walde T., Karhausen K.-F. The formation of edge cracks during rolling of metal sheet. *Steel Research International* 2007, 78 (10-11): 818-824.
- [25] Ko D.C., Lee S.H., Kim D.H., Byon S.M., Park H.D., Kim B.M. Design of sizing press anvil for decrease of defect in hot strip. *Journal of Materials Processing Technology* 2007, 187-188: 738-742.
- [26] Burton D. S., Gao X., Brinson L.C. Finite element simulation of a self-healing shape memory alloy composite. *Mechanics of Materials* 2006, 38: 525-537.
- [27] Awais M., Lee H.W., Im Y.T., Kwon H.C., Byon S.M., Park H.D. Plastic work approach for surface defect prediction in the hot bar rolling process. *Journal of Materials Processing Technology* 2008, 201(1-3): 73-78.
- [28] Son I.H., Lee H.D., Choi S., Lee D.L., Im Y.T. Deformation behavior of the surface defects of low carbon steel in wire rod rolling. *Journal of Materials Processing Technology* 2008, 201(1-3): 91-96.
- [29] Ervasti E., Ståhlberg U. Behavior of longitudinal surface cracks in the hot rolling of steel slabs. *Journal of Material Processing Technology* 1999, 94(2): 141-150.
- [30] Ervasti E , Ståhlberg U. Transversal cracks and their behavior in hot rolling of steel slabs. *Journal of Material Processing Technology* 2000, 101(1) : 312-321.
- [31] Yukawa N., Ishikawa T., Yoshida Y., Koyachi A. Influence of rolling condition on deformation of surface micro-defect in plate rolling. *Tetsu-to-Hagané* 2005, 91(12): 861-867.
- [32] Yukawa N., Yoshida Y., Ishikawa T. Deformation analysis of longitudinal surface micro-defects in flat rolling. *Tetsu-to-Hagané*, 2006, 92(11): 19-24.
- [33] Liu X.H.. Rigid finite element method and its application in rolling process. *Metallurgical Industry Press, Beijing*, 1994. (in Chinese)
- [34] Sun Y.K.. Numerical models in hot flat continuous rolling. *Metallurgical Industry Press, Beijing*, 1979.(in Chinese)

- [35] Wang M., Yang H., Sun Z.C., Guo L.G., Qu X.Z. Dynamic explicit FE modeling of hot ring rolling process. *Transactions of Nonferrous Metals Society of China* 2006, 16: 1274-1280.
- [36] Yu H.L., Liu X.H. Thermal-mechanical FE analysis of evolution behavior of slab surface cracks during hot rolling, *Materials and Manufacturing Processes*, 2009, 24(5): 570-578.
- [37] Wei D., Han J., Jiang Z.Y., Tieu A.K. A study on crack healing in 1045 steel. *Journal of Materials Processing Technology*, 2006, 177(1-3): 233-237.
- [38] Zhou Y., Guo J., Gao M., He G. Crack healing in a steel by using electropulsing technique. *Materials Letters* 2004, 58(11): 1732-1736.
- [39] Xiong, S.W., Rodrigues, J.M.C. and Martins, P.A.F. Three-dimensional modeling of the vertical-horizontal rolling process. *Finite Elements in Analysis and Design*, 2003, 39: 1023-1037.
- [40] Jiang, Z.Y., Tieu, A.K. and Lu, C. Mechanical modeling of friction variation in slab edging with a finite element method approach, *Tribology International*, 2004, 37: 733-742.
- [41] Yu H.L., Liu X.H., Li C.S. FEM analysis to the slab corner metal flow condition during multi-pass V-H rolling process, 2005, 26(10): 982-985. (in Chinese)
- [42] Xie H., Xiao H., Zhang G., et al. Analysis on rolling pressure distribution of strip width different reductions by explicit dynamic FEM, *Journal of Iron Steel Research*, 2002, 14(6), 33-35.(in Chinese)
- [43] Ding G.: Algorithms and methods of ANSYS/LS-DYNA, Beijing Institute of Technology, Beijing, 1999, pp.104.
- [44] Yu H.L., Liu X.H., Zhao X.M., Kusaba Y. FEM Analysis for V-H rolling process by updating geometric method. *Journal of Materials Processes Technology*, 2006, 180(1-3): 323-327.
- [45] Yu H.L., Liu X.H., Li C.S., Lan F.F., Wang G.D. Research on the behavior of transversal crack in slab V-H rolling process by FEM. *Journal of Materials Processes Technology*, 2009, 209(6): 2876-2886.
- [46] Yu H.L., Liu X.H., Ren X.J. Behavior of longitudinal cracks in slab V-H rolling processes. *Steel Research International*, 2008, 79(7): 537-543.
- [47] Cai K.K., Han C.J., Sun Y.H. Crack control during continuous casting. *Conference on the Continuous Casting Slab Technology*, Nanjing, 2006, 1-15. (In Chinese)
- [48] Yu H.L., Liu X.H., Jiang Z.Y. FE analysis of behavior of internal-longitudinal cracks in slab during vertical-horizontal rolling. *Proceeding of The 8th Asia Pacific Conference on Materials Processing*, 2008, 6, Guilin-Guangzhou, China, p.799-804.
- [49] Liu X.H., Yu H.L. Analysis of crack healing in hot rolled deformed piece. *Journal of Iron and Steel Research*, 2009, 21(6): 38-41. (in Chinese)
- [50] Yu H.L., Liu X.H., Li C.S., Zhao X.M., Kusaba Y. Influences on the plastic strain distribution of slab of vertical roll shape during multi-pass V-H rolling process. *Acta Metallurgical Sinica.(English Letters)*, 2006, 19(1): 51-56.
- [51] Matsumiya T., 2006. Recent topics of research and development in continuous casting. *ISIJ Int.* 46(12), 1800-1804.
- [52] Todoroki H., Mizuno K., 2004. Effect of silica in slag on inclusion compositions in 304 stainless steel deoxidized with aluminum. *ISIJ Int.* 44(8),1350-1357.

- [53] Luo C.H., Ståhlberg U., 2001. Deformation of inclusions during hot rolling of steels. *Journal of Material Processing Technology* 114, 87-97.
- [54] Luo C.H., Ståhlberg U., 2002. An alternative way for evaluating the deformation of MnS inclusion in hot rolling of steel. *Scand. J. Metall.* 31(1), 184-190.
- [55] Ervasti E., Ståhlberg U., 2005. Void initiation close to a macro-inclusion during single pass reductions in the hot rolling of steel slabs: A numerical study. *Journal of Material Processing Technology* 170, 142-150.
- [56] Hwang Y.M., Chen D.C., 2003. Analysis of the deformation mechanism of void generation and development around inclusions inside the sheet during sheet rolling process. *Proc. Instn Mech. Engrs Part B: J. Eng. Manuf.* 217(10), 1373-1381.
- [57] Melander A., 1997. A finite element study of short cracks with different inclusion types under rolling contact fatigue load. *Int. J. Fatigue.* 19(1), 13-24.
- [58] Zhang S.T., 2001. *Steel Materials Handbook- Stainless Steel*, Standards Press of China, Beijing.
- [59] Li R.J., 1995. *Ceramic-Metal Complex Materials*, Metallurgical Industry Press, Beijing.
- [60] Yu H.L., Liu X.H., Bi H.Y., Chen L.Q. Deformation behavior of inclusions in stainless steel strips during multi-pass cold rolling. *Journal of Materials Processing Technology*, 2009, 209(1): 455-461.
- [61] Yu H.L., Bi H.Y., Liu X.H., Chen L.Q. Numerical analysis of movement of inclusion in stainless steel during cold rolling. *Proceedings of First International Conference of Modelling and Simulation, Vol.V, Modelling and Simulation in Mechanics and Manufacture, Nanjing, China, 2008, 8: 486-491.*
- [62] Wei D.B., Han J. T., Tieu K., Jiang Z.Y.. Simulation of crack healing in BCC Fe. *Scripta Mater*, 2004, 51(6) , 583-587.
- [63] Yu H.L., Liu X.H., Li X.W. Crack healing in low carbon steels under hot plastic deformation. *Materials and Manufacturing Processes*, 2010, 25(4), in publish.
- [64] Ma Q.X., Wang Z.C., Zhong Y.X. The mechanism of faults originating from inclusions in the plastic deformation process of heavy forging. *Journal of Material Processing Technology*, 2002, 123: 61-66.
- [65] Zhang G.P., Takashima K., Higo Y.. Fatigue strength of small-scale type 304 stainless steel thin films. *Mater. Sci. Eng. A*, 2006, 426: 95-100.
- [66] Wang A., Thomson P.F., Hodgson P.D. A study of pore closure and welding in hot rolling process. *Journal of Material Processing Technology* , 1996, 60: 95-102.
- [67] Yu H.L., Bi H.Y., Liu X.H., Tu Y.F. Strain distribution of strips with a spherical inclusion during cold rolling. *Transactions of Nonferrous Metals Society of China*, 2008, 18(4): 919-924.
- [68] Yu H.L., Liu X.H., Li X.W. Analysis of inclusion deformation and crack generation during rolling with a super-thin layer by FEM. *Materials Letters*, 2008, 62(10-11): 1595-1598.
- [69] Xue Z.L., Weng Y.Q., Li, Z. B. Zero inclusion steel and its oxide inclusion behavior. *World Iron & Steel* , 2008, 8(4): 17-20. (in Chinese)
- [70] Zhao Z.Y., 1999. *Mechanics in Metal Forming*, Metallurgical Industry Press, Beijing.
- [71] Yu H.L., Bi H.Y., Liu X.H., Chen L.Q., Dong N.N. Behavior of inclusions with weak adhesion to strip matrix during rolling using FEM, *Journal of Materials Processing Technology*, 2009, 209(9): 4274-4280.



Finite Element Analysis

Edited by David Moratal

ISBN 978-953-307-123-7

Hard cover, 688 pages

Publisher Sciyo

Published online 17, August, 2010

Published in print edition August, 2010

Finite element analysis is an engineering method for the numerical analysis of complex structures. This book provides a bird's eye view on this very broad matter through 27 original and innovative research studies exhibiting various investigation directions. Through its chapters the reader will have access to works related to Biomedical Engineering, Materials Engineering, Process Analysis and Civil Engineering. The text is addressed not only to researchers, but also to professional engineers, engineering lecturers and students seeking to gain a better understanding of where Finite Element Analysis stands today.

How to reference

In order to correctly reference this scholarly work, feel free to copy and paste the following:

Hailiang YU (2010). FE Analysis of Evolution of Defects during Rolling, Finite Element Analysis, David Moratal (Ed.), ISBN: 978-953-307-123-7, InTech, Available from: <http://www.intechopen.com/books/finite-element-analysis/fe-analysis-of-evolution-of-defects-during-rolling>

INTECH
open science | open minds

InTech Europe

University Campus STeP Ri
Slavka Krautzeka 83/A
51000 Rijeka, Croatia
Phone: +385 (51) 770 447
Fax: +385 (51) 686 166
www.intechopen.com

InTech China

Unit 405, Office Block, Hotel Equatorial Shanghai
No.65, Yan An Road (West), Shanghai, 200040, China
中国上海市延安西路65号上海国际贵都大饭店办公楼405单元
Phone: +86-21-62489820
Fax: +86-21-62489821

© 2010 The Author(s). Licensee IntechOpen. This chapter is distributed under the terms of the [Creative Commons Attribution-NonCommercial-ShareAlike-3.0 License](https://creativecommons.org/licenses/by-nc-sa/3.0/), which permits use, distribution and reproduction for non-commercial purposes, provided the original is properly cited and derivative works building on this content are distributed under the same license.

IntechOpen

IntechOpen